A Glued Ultra-High Vacuum Cell Using Titanium and Fused Silica and a High Resolution Optical Setup for Ultracold Atom Experiments

Valerie Leu

Bachelorarbeit in Physik
angefertigt im Institut für Angewandte Physik

vorgelegt der
Mathematisch-Naturwissenschaftlichen Fakultät
der
Rheinischen Friedrich-Wilhelms-Universität
Bonn

Oktober 2023

Ich versichere, dass ich diese Arbeit selbstständig verfasst und keine anderen als die angegebenen Quellen und Hilfsmittel benutzt sowie die Zitate kenntlich gemacht habe.

Bonn, 02.10.2023 .....
Datum

.....
Unterschrift

1. Gutachter: Prof. Dr. Sebastian Hofferberth
2. Gutachterin: Dr. Nina Stiesdal

Acknowledgements

I would like to thank all members of the Nonlinear Quantum Optics group, who very kindly accepted me into their group and were always incredibly helpful. Thank you for teaching me so much in this past few months. I want to especially thank Prof. Sebastian Hofferberth, who made it possible for me to write my bachelor thesis in his group and who in the first place inspired me to write bachelor thesis in a quantum optics group with his amazing "Experimental Physik 4" lecture. I would very much like to thank Nina Stiesdal, who always had a helpful advise and also kindly agreed to be my second examiner for this thesis. A special thanks also to Hannes Busche and Cedric Wind, who supported me every day of this past few month in so may ways, that they can not all possibly be listed here. They really had a solution to every possible problem, I could not master myself. Thank you, Julia Gamper and Valerie Mauth for being the best lab mates one could wish for. I will miss working in the lab with you. I also really want to thank Tina Naggert and again Prof. Sebastian Hofferberth, who made sure, I had someone to talk to during a hard time. A special thank as well to all people, who proof read my thesis and gave me useful feedback. And last but not least I would like to thank my family, my boyfriend and my friends, who always believe in me and cheer me up. I would not be anywhere near, where I am now, without your support.

Contents

CHAPTER 1

Introduction

Ultracold atoms are a popular platform for both applied and fundamental quantum physics. Experiments in this field rely on ultra-high vacuum (UHV) and require a good optical access, as well as high quality optics, as atoms have to be trapped and manipulated using laser beams.

The Nonlinear Quantum Optics group is particularly interested in Rydberg atoms. Rydberg atoms are highly excited atoms, which interact strongly with each other via dipolar interactions [1, 2]. Hence they can be used for qubits. This uses the phenomen of the Rydberg blockade, which prevents any other Rydberg excitation with the same laser in a distance of a few µm of an already excited Rydberg atom [3].

Using the experience of the Rubidium Quantum Optics project (RQO) [4], the Hybrid Quantum Optics (HQO) experiment plans to combine nonlinear quantum optics, which is based on the strong dipolar interaction of Rydberg rubidium atoms, with other quantum systems, such as electro-mechanical oscillators, which operate in the microwave regime [5]. The oscillator can be coupled to superconducting qubits, such that a combination of all these approaches may be used to couple optical photons to superconducting qubits [6].

For this system to work, the mechanical mode of the oscillator is cooled to near its quantum ground state [7]. In the HQO experiment we plan to get close to this regime using a cryogenic ultracold atom apparatus, which cools the chip with the oscillator down to 4 K. The atoms get trapped over the oscillator in the magnetic field of the wires integrated into the chip [8]. In the experiment only a one dimensional chain of Rydberg atoms is supposed to be trapped, which can be done by using the Rydberg blockade mentioned before, if the 780 nm and 480 nm lasers, which are used to excite the Rubidium atoms in a two-photon transition, are focused $\lesssim 10\,\mu$m above the chip [5].

More generally, any atom trapping requires ultra-high vacuum (UHV) to prevent atom loss due to background collisions. This is because the trap lifetime of trapped atoms is getting shorter the more background collision are happening [9].

In Chapter 2 the process of building a fused silica titanium vacuum cell for such UHV and the testing of its optical and vacuum characteristics is described. In the Nonlinear Quantum Optics group a vacuum cell with NBK7 glass and a titanium frame was successfully realized in the past. But especially for high power light ($\gg 1$ W), i.e. for optical dipole traps [10], NBK7 is only suitable to a limited extent, because of thermal lensing, that is caused by light absorption in the glass. With the test cell described in Chapter 2 it was tested, if it is also possible to use fused silica glass instead, as it has better characteristics regarding thermal lensing [11]. But fused silica glass brings the problem, that the coefficient of thermal expansion (CTE) of the glass is very different to the CTEs of titanium. That could lead to the adhesion

not holding or stress being introduced to the glass, which could lead to birefringence. There are also vacuum glass chambers, that can be bought ready to use and have a good optical quality, but they are limited in size and shapes. Commercial viewports with a glass metal seal are often problematic, as they are very big and bulky. The tests in Chapter 2 have shown, that a test cell with titanium and fused silica can be build without leaks, but significant birefringence was observed introduced by the windows.

But not only the glass of the vacuum chamber has to be carefully constructed, the optics surrounding the vacuum chamber have to be of high quality as well and the setup has to be well aligned. The main components, which required focussing of the 780 nm laser to 8 µm, for the Rydberg excitation laser setup, like the achromatic lens, were already chosen and characterized in Samuel Germer's bachlor thesis [12]. In Chapter 3 it was started to build the setup with the realistic dimensions, taking the space constrains around the experiment into account. Doing so the quality of the optics was tested and the polarization of the used laser was set. The polarization could be set well and the focussing of the 780 nm laser to 8 µm was achieved.

CHAPTER 2

Self-build Titanium Fused Silica Test Cell

In this chapter it is explained, how Fused Silica glass windows were glued to a titanium frame to build a vacuum chamber. This is done to test, if Fused Silica glass can be used to build such vacuum chambers instead of NBK7 glass, that previously was used in this group for self-glued cells. In Section 2.1 a short motivation is given, as to why to glue a vacuum cell instead of buying a ready one. The properties of the different materials, that can be used for such a vacuum chamber, are compared to each other in Section 2.2. Before the windows can be glued to the frame, all parts, that are used in the gluing procedure, have to be made vacuum clean. The cleaning process is described in Section 2.3. The actual gluing process is shown in Section 2.4. To see how successful the gluing process was, it was tested which vacuum level the chamber could reach in Section 2.6 and in Section 2.7 the windows were tested for their optical quality before and after the gluing process.

2.1 Motivation

For a lot of experiments UHV chambers with optical accessibility are needed. An UHV is reached, when the pressure inside of the chamber is located between 10^{-7} mbar and 10^{-12} mbar [13]. The mean free path of a particle in that vacuum ranges from 10^{3} m to 10^{8} m. To get UHV in a chamber, the chamber has to be tight on this scale of pressure. As the chamber has to be big enough for all possible measurements and also has to provide a good optical access, like big windows, there are certain challenges to the design process.

There are vacuum cells that can be commercially obtained. For instance UHV glass cells, like seen in Fig. 2.1, can be bought from ColdQuanta [14]. Those cells are made completely out of glass up to the flanges, which provides a great accessibility. But they are only build up to a certain size. There is also a set construction, that can only be attached to the experiment by one side, as attaching it with both sides would lead to too much tension on the glass. That limits the way, the cell can be build into experiments.

Another option is a cell by own design with round viewports screwed onto it, like those from Pfeiffer Vacuum [15]. That way the size and general design of the the cell is not limited, but the optical accessibility is reduced compared to the cells from ColdQuanta. But even more important is, that those viewports are very big and bukly. This is a problem for the HQO experiment, as the volume inside of

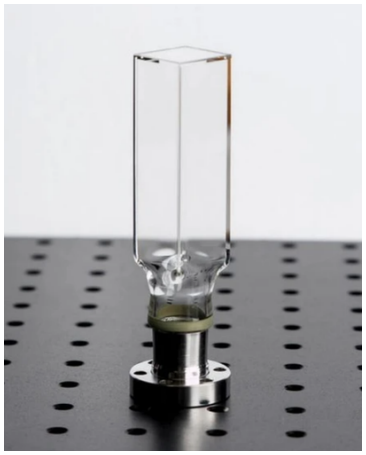

Figure 2.1: 2 cm Thin-Walled Cell from ColdQuanta [14]

the cell has to be as big as possible, while the chamber itself should be as small as possible. This is because the magnetic wires have to be very close to the atoms to provide a good magnetic transport, as the magnetic field scales with $\sim \frac{1}{r^3}$.

With the right techniques it is possible to build vacuum chambers with good optical access, that are much more flexible in the design choices than commercial obtained ones. Relaying on the experiences of the Ytterbium Quantum Optics (YQO) group, the HQO group build their own vacuum chamber, consisting of NBK7 glass windows glued onto a titanium frame. As previously mentioned, gas inclusions in the NBK7 glass lead to thermal lensing, especially for high energy light, like $\gg 1$ W. Fused Silica glass windows promise less inclusions in the glass, but also have a CTE, which is more different from the CTE of titanium than the CTE of NBK7 is. To test, if this might lead to the adhesion breaking or briefringence in the glass, because of stress, this self-build titanium fused silica test cell was glued.

2.2 Design considerations

When designing a chamber for an UHV, one has to pay especially close attention to the choice of material as there are several aspects one has to consider in the selection process, like the outgassing and the tightness of those materials.

For a lot of cells stainless steel and BK7 glass are the most common components. Stainless steel is a good candidate, because it is a firm metal with a high corrosion resistance that can be used at high temperatures [13].

BK7 is a relatively inexpensive hard glass with high transmission for light from the visible to the near infrared [11]. It has a low bubble and inclusion content and is therefore very suitable for transmission optics, as those inclusion absorb high-energy light. This absorption leads to the glass heating up and therefore to thermal lensing, which changes the beam pointing. However UV graded Fused Silica is of even higher purity than BK7 glass. It can safely be used with high-energy lasers, because of its lower inclusion content. This lower inclusion content also leads to a higher transmission at lower wavelengths. Fused Silica glass already reaches a transmission of 80% of the incoming light at 180 nm, whereas

N-BK7 glass only reaches it around 380 nm [11].

It is also important that the outgassing of the used materials is sufficiently small. Reaching a pressure below 10^{-6} hPa, gases inside of most plastics will start to diffuse to the surface and particles on the surface disorp into the vacuum [13]. This disorption does also happen to gases on the surface of glass or metal parts, but the diffusing of gases inside these materials starts to have an impact at lower pressures. The amount of gas diffusing and disorping can be drastically raised by heating the cell up to sometimes several hundred Celsius, which is called "baking out". Most of the gases inside of the walls of the chamber diffuse to the outside during that process. Afterwards the pressure inside off the cell can be pumped down to much lower pressures, as there is less gas inside of the walls, that can diffuse to the inside.

Heating up the chamber brings a new condition the cell has to meet. The CTEs of the used materials have to be approximately in the same scale. If the CTEs do not match, the volumes of the materials expand differently when they are heated, which leads to stress and in the worst case to the adhesion breaking. The CTE of stainless steel is relatively high, whereas the CTE of N-BK7 and Fused Silica glass is comparatively low, which is why we are using titanium, which has a lower CTE than stainless steel. The Fused Silica glass has a lower CTE than the N-BK7 glass, which results in a greater difference between the CTEs of the Titanium and the Fused Silica glass, which is why it has to be tested, if it is still possible to use the Fused Silica glass. The CTEs can be seen in Table 2.1.

Table 2.1: CTE's of materials for vacuum chambers [13, 16–19]

	CTE	
EPO-TEK H77S Glue	below 80 °C:	$38.59 \cdot 10^{-6}$ 1/K
	above 80 °C:	$95.445 \cdot 10^{-6}$ 1/K
Stainless Steel	20 °C - 300 °C:	$17.0 \cdot 10^{-6}$ 1/K
Titanium	at 20 °C:	$8.9 \cdot 10^{-6}$ 1/K
N-BK7 Glass	−30 °C - 70 °C:	$7.1 \cdot 10^{-6}$ 1/K
	20 °C - 300 °C:	$8.3 \cdot 10^{-6}$ 1/K
Fused Silica Glass	0 °C - 100 °C:	$5.1 \cdot 10^{-7}$ 1/K
	0 °C - 200 °C:	$5.8 \cdot 10^{-7}$ 1/K
	0 °C - 300 °C:	$5.9 \cdot 10^{-7}$ 1/K

In Fig. 2.2 the CAD design of the test-cell with a DN63 flange can be seen. For the test-cell titanium grade 2, UV graded fused silica windows and the EPO-TEK H77S glue were used.

2.3 Vacuum Cleaning

In preparation for the actual gluing process all screws, every tool, that could get in contact with the chamber, and all components for the cell have to be made vacuum-clean, since organic residue like oil, fingerprints or hair and dust will outgass in an UHV environment and increase the pressure.

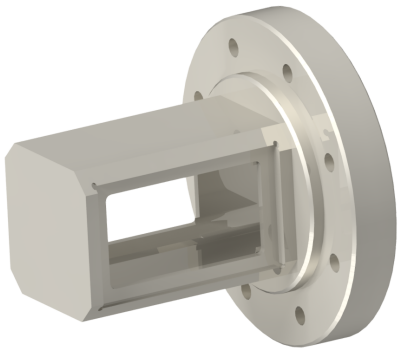

Figure 2.2: CAD design of the self-glued test-cell

The following elements had to be cleaned:

- titanium frame
- flange adapter for the vacuum pump
- small scissor pliers
- big scissor pliers for grabbing bigger vacuum parts
- M6 and M8 screws
- aluminium mounts for the cell

When cleaning those part, oneself should be "vacuum clean" too. One should always wear close-fitting clothes in order to avoid loose sleeves touching vacuum parts without being noticed. More importantly one should be wearing hairnets and powder free gloves at all times. Keeping track on what was last touched and thus the degree of purity of the worn gloves is essential, as the gloves have to be changed after touching something not vacuum-clean. But during the cleaning process it got apparent that the top layer of the gloves gets dissolved by the chemicals. When touching an object after that, residue settled on the surface. To fix this problem the scissor pliers were cleaned before the other components. With these pliers the wet parts could be moved without touching them with the gloves.

The components, that are getting cleaned, are put into beakers or metal containers, which are filled with the chemicals and then put into an ultrasonic bath. Only high purity optics grade solvents with very low evaporation residue should be used is the cleaning procedure. The chemicals can be tested for their purity by putting a small droplet of the solvent on a test optic like a small mirror and observing the evaporation residue of the droplet.

In the first step the elements separately get sonicated in distilled water with soap at 70 °C for an hour to get rid of any oil [20]. The Sonoswiss Cleaner T1(SW-CT1) is used in a 3-8% solution to clean hard metals in this case the titanium frame [21], while the Sonoswiss Cleaner T2(SW-CT2) gets used in a 2-5% solution for soft metals like aluminium [22]. To get rid of the soap and loose dirt, the elements then need to be rinsed off with distilled water and have to be sonicated again for ten minutes, but only in distilled water [20]. After that one sonicates the parts in aceton for an hour. Aceton is a really agressive

solvent, but leaves behind the dissolved dirt when it evaporates. That is why the components must be rinsed with isopropanol before the aceton can evaporate. Following the rinsing with isopropanol the pieces are sonicated for 15 minutes in isopropanol as well. To make sure the isopropanol does not evaporate leaving behind any residue, the objects get blown off with compressed air.

Clean parts have to be safely stored away by wrapping them in aluminium foil [20]. During the whole procedure it is important to pay special attention to the knife-edges of the flanges, because a flange with a scratched knife-edge is unusable. The knife-edge does not cut into the gasket at that point, which leads to a leak. Hence the parts with kife-edges should, if possible, not be put in the aluminium foil with their edges facing towards the foil.

2.4 Gluing

The EPO-TEK H77S glue, that was used for the gluing in the next step, is a two-component epoxy [16]. Two-component epoxies usually consist of a hardener and the epoxy resin, which have to be mixed [23]. The chemical reaction between the two components of the glue forms a very strong bond [24]. Which is why one has to take special care of the mixing ratio. EPO-TEK specifies a mixing ratio by weight of 100:35 in the data sheet of the epoxy [16].

The components have to be mixed very thoroughly for the best result. During the mixing process air bubbles can get enclosed in the glue. If not removed, those bubbles could weaken the adhesion, as the surface area is reduced, or form virtual leaks. Virtual leaks are cavities, that only evacuate very slowly and therefore form a constant gas source, like a leak. To avoid this, the glue can be evacuated under a vacuum to remove the remaining air in the glue. There are also other possibilities to get rid of the bubbles, like sonicating the glue. Both possibilities were available, which is why they were both tested.

In the first approach the beaker with the glue was placed in a pot, which then got covered with a glass plate. Through a hole in the plate the pot got evacuated with a vacuum pump. Due to the air inside the glue, the glue started rising. This can be seen in Fig. 2.3. One has to make sure, that the glue does not rise above the beaker and touches the outside of it or the inside of the pot, which is not clean. Therefore one can pause the pumping process until enough bubbles popped. The degassing process can be stopped when only a few small bubbles remain in the glue, as seen in Fig. 2.4(b).

The second method for degassing the glue to be investigated is sonication of the glue. After the glue was sonicated, we noticed, that the glue had separated into to parts, as seen in Fig. 2.4(a).

Overall the method using only the sonicator proved to be insufficient. Degassing the glue in a vacuum worked well.

The titanium frame can not stand horizontal on its own. But when the frame is tilted, the glue will run to one side of the frame. To prevent that from happening, the frame has to be supported. The construction shown in Fig. 2.5 was used for this test cell. Two bars got screwed onto the flange of the test cell and a plastic board, which leads to a secure, horizontal position of the frame.

The glue has to be spread over the whole surface, where the windows will be laid down, to guarantee the best adhesion. While spreading the glue, one has to make sure, that the glue layer is thin, because of the CTE of the glue. Additionally too much glue could lead to the glue running into the cell. The

Figure 2.3: The glue for the first window expanding in the vacuum.

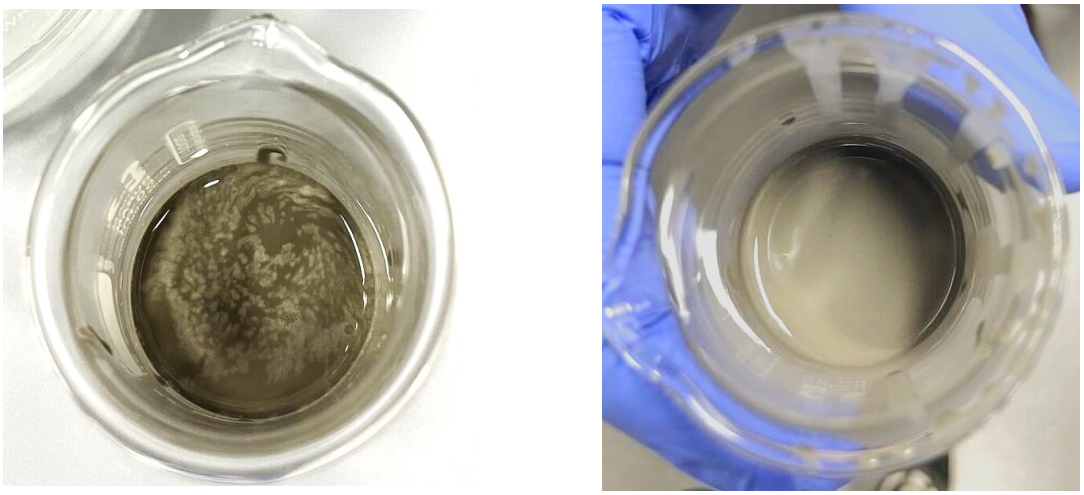

(a) glue after being sonicated

(b) glue after being evacuated

Figure 2.4: Sonicating vs evacuating the glue for the second window.

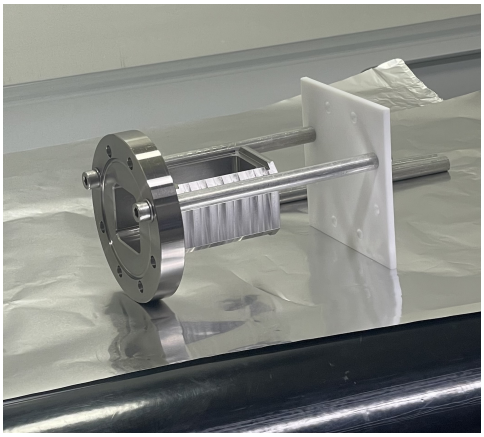

Figure 2.5: Construction for holding the titanium frame in a horizontal position.

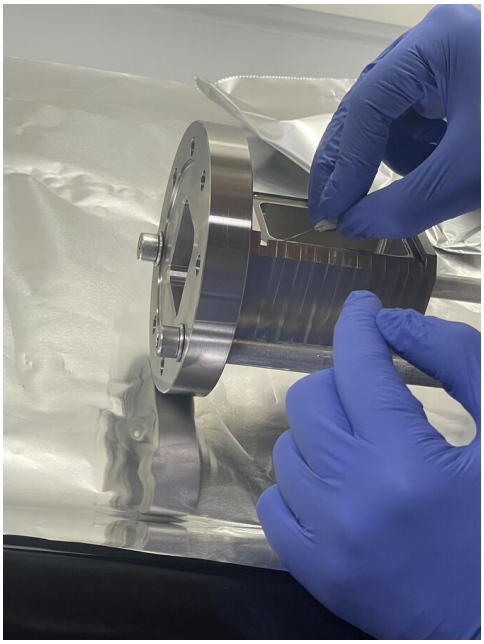

Figure 2.6: Spreading the glue with a needle.

layer should also be as evenly distributed as possible. This is because the outer edges of the glue touching the walls of the cell are higher, because of the surface tension. If the glue is well distributed, the inner edges will be below the outer ones. That is wanted, because when putting the windows down onto the glue, the wetting will start on the outer edges and move towards the inside without air getting trapped. The easiest solution is to fill the glue into a syringe and spread it with a needle, as seen in Fig. 2.6

The first window was put onto the titanium frame instantly after spreading the glue. On the second window the "piezobrush® PZ3" was tested, before the window was put onto the glue.

The "piezobrush® PZ3" is a plasma-device, that can be used by hand [25–29]. It creates cold active

Figure 2.7: Plasma treatment of the second window for better adhesion.

atmospheric-pressure plasma at a low temperature, which makes it possible to increase the surface energy of materials. The plasma consists of neutral and cold gas, which has a few electrons and ions in it. These electrons and ions collide with the gas molecules and create molecules with metastable states, which makes the plasma highly chemically reactive. On the glass the plasma produces polar molecular anchor groups. Those anchor groups correlate with those in the glue. Expressed differently, the plasma increases the surface tension of the treated glass, which also enhances the adhesion of the glue to it, because the surface energy gets bigger than the surface tension of the glue.

The usage of the plasma-device is simple. The device has to be moved with a distance of a few centimeters over edge of the glass, where the glue will touch it (see Fig. 2.7).

The windows have to be put down carefully as to trap as few air bubbles as possible between the glue and the glass. Despite being very carefully still one to two bubbles were trapped. That is probably because the glue was not spread well enough. As one can see in Fig. 2.8, the bubbles are not near the inside of the cell and therefore not at risk of becoming virtual leaks. Additionally they are small enough to not impair the adhesion.

After placing the window, the cell gets put into the oven. The glue has to be cured at 150 °C for an hour, which can be seen in the data sheet of the glue [16]. The oven has to be heated up with a ramp as the used materials of the chamber not only have different CTE's but also differ in their Thermal Conductivity as seen in Table 2.2. I.e the titanium frame will reach the surrounding temperature faster than the glass. That is why it will not only expand more, because of its CTE, but also faster. Leading to even greater tension between the frame and the windows, if the oven does not get heated slowly. The smallest ramp of the oven in the FTD is 1 °C per minute, which is why it was chosen. After the curing the oven gets cooled down with the same ramp again.

As an additional precautionary measure against dust depositing on the cell during the curing process,

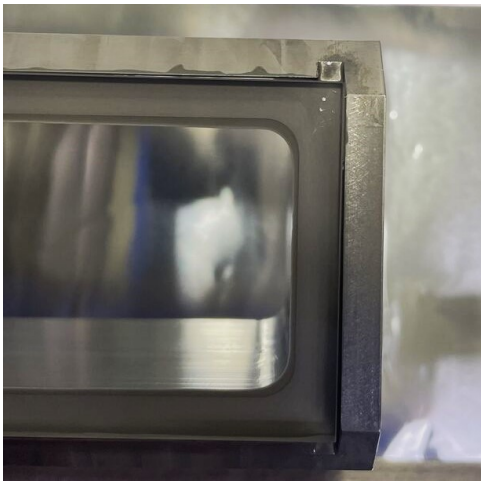

Figure 2.8: Air bubble (on the right side at the top) that formed when placing the first window.

Table 2.2: Heat conductivity of the used material for the test cell [16, 17, 19]

Material	Heat Conductivity	
Titanium	at 20 °C	20 $^{W}/_{m\,K}$
Fused Silica Glass	at 20 °C	1.38 $^{W}/_{m\,K}$
EPO-TEK H77S Glue	no specified temerature given	0.7 $^{W}/_{m\,K}$

it was covered with aluminum foil (see Fig. 2.9).

2.5 Visual inspection of gluing results

The results after taking the chamber out of the oven can be seen in Fig. 2.10.

On both windows the glue opposite of the flange is brighter. The discoloration at only one side of the windows indicates that the frame was not held precisely horizontal using the mount. To prevent this in the future, a more precise mount should be used.

Additionally, the first window shows a pronounced rainbow pattern on the bright side. At first sight no such pattern could be observed on the second window. Later a faint rainbow pattern could as well be seen on the second window at the place with lighter colour (see Fig. 2.11). It could not be examined where exactly this pattern comes from. It could be that the glass came off of the glue at that place, because of deformation of the glass. On the second window this rainbow pattern is only very faint, which suggests that the second window did deform as well, however the glue did probably not part from the window but from the frame this time.

If those assumptions are right, the plasma actually did improve the adhesion of the glue to the window. The next step to test this could be to use the plasma on the windows as well as on the titanium frame. Aside from that, one could also use a weight to press the windows down onto the frame, while heating the cell up. That could prevent the deformation of the glass.

(a) cell without foil

(b) cell covered with foil

Figure 2.9: Test cell gets covered with aluminium foil to make sure it stays clean in the oven.

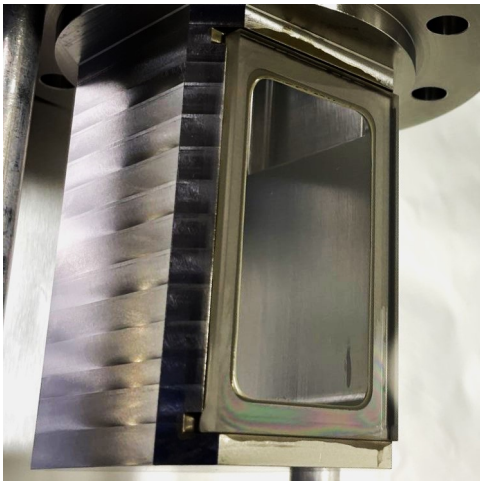

(a) first window

(b) second window

Figure 2.10: The windows of the test cell after curing the glue.

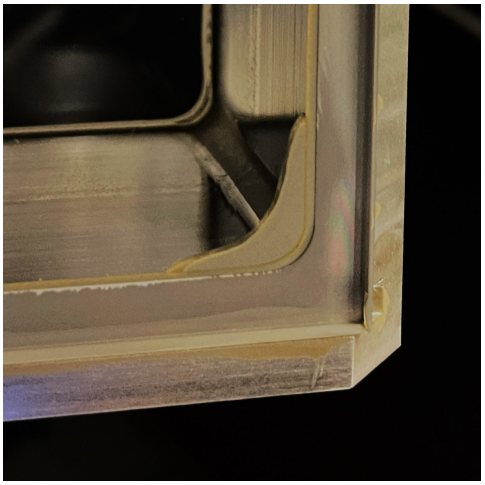

Figure 2.11: A faint rainbow pattern can be seen on the second window.

Figure 2.12: Test cell connected via a DN40 bellow to a vacuum pump stand consisting of a "MVP 040-2" vacuum backing pump and a turbo pump of type "HiCube 80 Classic".

2.6 Testing the Vacuum inside of the Test-Cell

It has to be tested to which scale the vacuum inside of the cell can go down and thus if the gluing process did work.

The cell was mounted onto an optical table and connected to the pump stand consisting of a MVP 040-2 vacuum backing pump and a turbo pump of type HiCube 80 Classic via a DN40 bellow, see Fig. 2.12.

Once the pump is safely placed onto the table the vacuum pump can get started.

The data of the pumping down can be found in Table A.1. For the pressure the data sheet of the used "pirani/cold cathode gauge PKR 360" gives an error of 30 % [30]. The error for the time is approximately

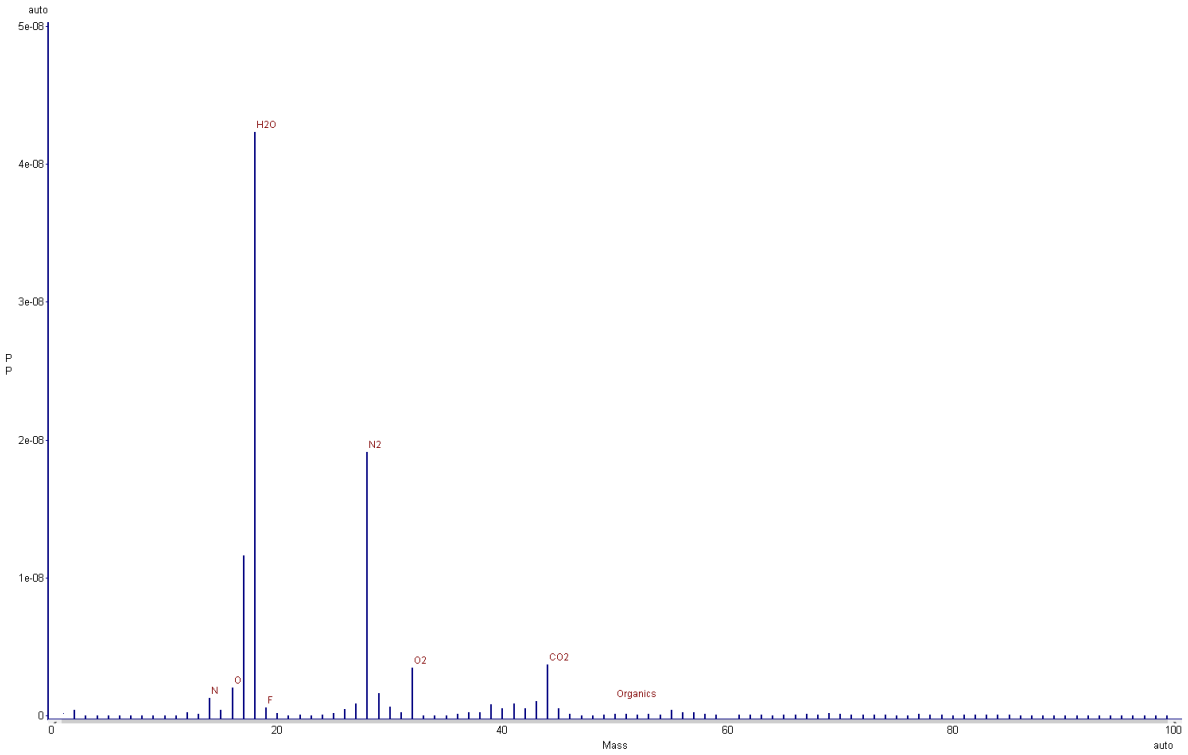

Figure 2.13: 1. mass spectrum of the vacuum inside the test cell
x-axis: mass given in [u]
y-axis: partial pressure given in [mbar]

2 s, because of the needed time to read off the time and the pressure. After approximately a day the pressure went down to $8.6 \cdot 10^{-8}$ mbar.

The total pressure in the vacuum system does not provide any information about the composition of the residual gases in the chamber. With the Residual Gas Analyzer (RGA) of the turbo pump, called "Pfeiffer Vacuum Model PrismaPro® QMG 250 F1", a vacuum diagnosis can be performed. The RGA is a quadrupole mass spectrometer (QMS) that can be used for high and ultra-high vacuum to determine a mass spectrum of the investigated vacuum, like seen in Fig. 2.13 [31]. By comparing the peaks of the mass spectrum with the fragmentation patterns of molecules saved in a library given by the RGA program, common species can be assigned to the peaks in the mass spectrum. That way one can check for any unwanted contamination in the vacuum.

The mass spectrum of the vacuum, as it is shown by the software of the RGA, can be seen in Fig. 2.13. There is a lot of H_2O, which one can only get rid of by baking out the cell. The peaks for N_2 and O_2 indicate that there is a leak, because their ratio resembles the composition of air, which is 78.090 % of nitrogen, 20.936 % of oxygen and 0.974 % of other substances[32].

To locate the position of the leak, a helium leak check has to be done. The RGA can also serve as an intrinsic leak detector [31]. In the program of the RGA the leak detection has to be started. The program now shows the partial pressure of the helium against the time. When helium gets close to a leak, a rise in

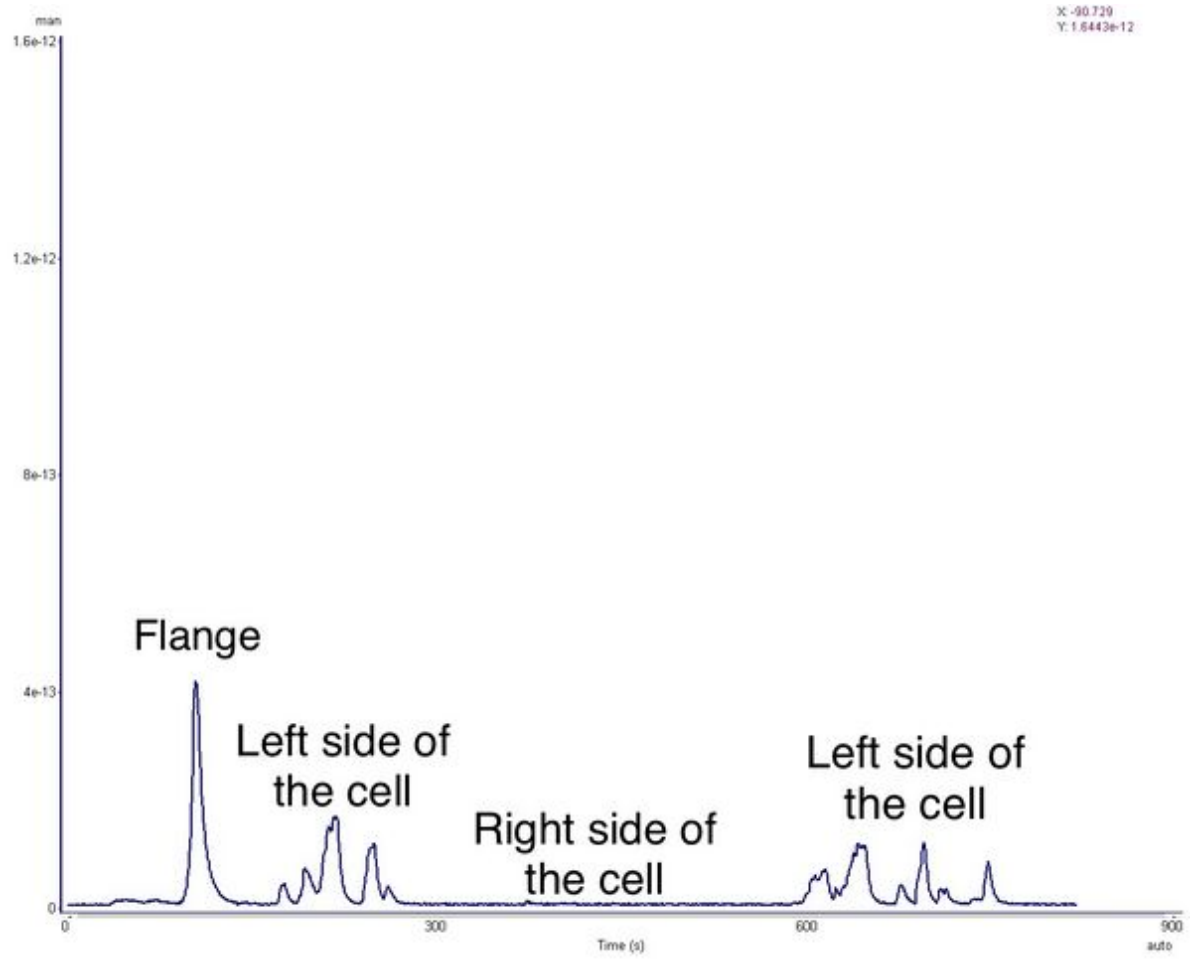

Figure 2.14: Helium leak test on the flange between the reducer and the bellow and on both windows.
x-axis: time given in [s]
y-axis: partial pressure given in [mbar]

pressure will be detected, as helium is an extremely volatile gas, that can go through even smallest gaps. A helium leak test was done on the flange and also on the sides of the window (see Fig. 2.14). As seen in Fig. 2.14 the flange still had to be tightened. The left window had small leaks at the places shown in Fig. 2.15. The window that is called left window in Fig. 2.14 is the window, that got glued second and got the plasma treatment.

To fix this leak the "330-VACSEAL-S" from allectra was used [33]. It is a silicone-based thin film sealant, that can be used for gluing materials with widely different CTE's at an vacuum level. The glue can be cured at 250°, but also at room temperature, which would take several days.

The glue got applied with a little brush onto the leaks. At first the cell was not heated up to cure the glue, but we did a leak test and a vacuum diagnostic on both of the windows and after letting the glue dry for a day. There are no more leaks. The glue already helped after a day, even tough it did not cure long enough.

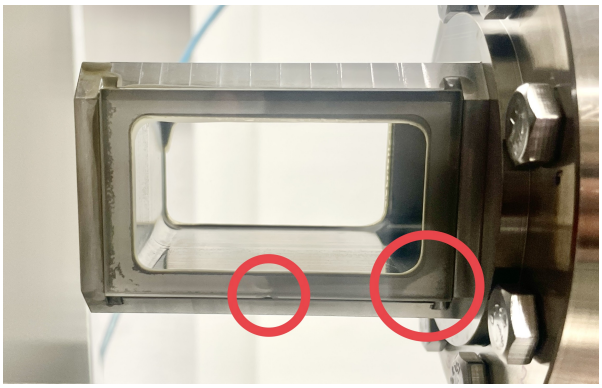

Figure 2.15: Places where leaks were detected on the left window.

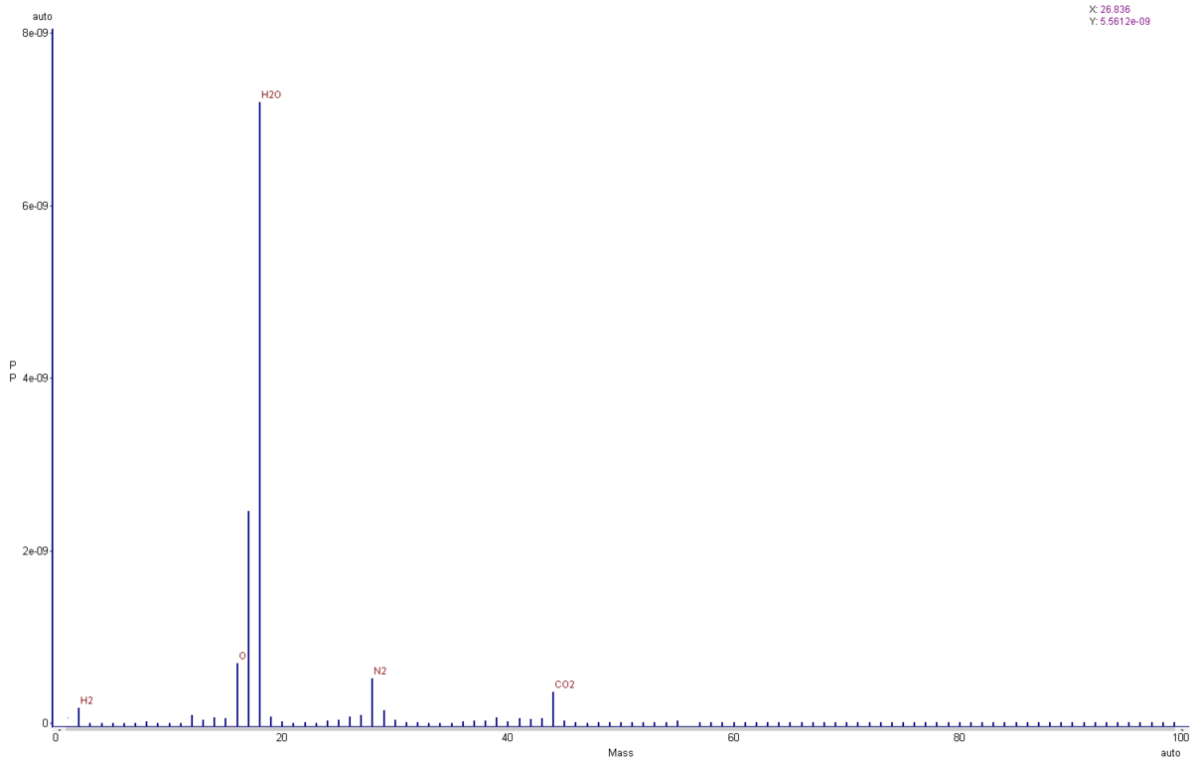

Figure 2.16: Second mass spectrum of the vacuum inside the test cell.
x-axis: mass given in [u]
y-axis: partial pressure given in [mbar]

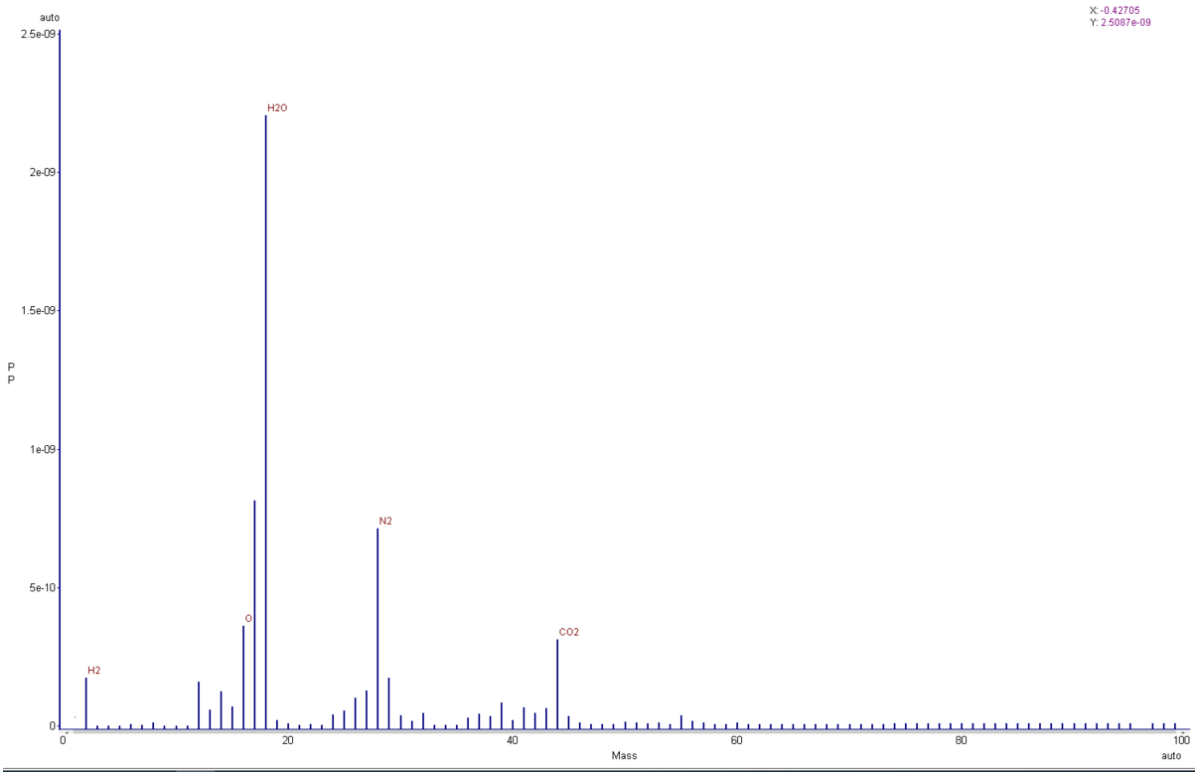

Figure 2.17: Final mass spectrum of the vacuum inside the test cell.
x-axis: mass given in [u]
y-axis: partial pressure given in [mbar]

There is still a lot of H_2O left. To get rid of the left H_2O and really put the cell under stress, the cell was baked again. As the "330-VACSEAL-S" did work really well on the leaks, we wanted to test, if it also helps to prevent leaks, when heating up the chamber again. That is why the glue got put all around the sides of the left window. Then the chamber got baked in the oven at 150 °C again.

After putting it on the optical table once more, the cell got connected to the turbo pump. The data of the pressures can be found in Table A.2. The errors are the same as for the data in Table A.1. Another leak test around the windows shows, that no additional leaks did appear. Looking at the mass spectrum in Fig. 2.17, one can see that the amount of H_2O went down. In conclusion the stress test was successful.

There was no difference between the window with the allectra glue and the one without. So no conclusion regarding that can be drawn other than that it did not harm to put it around the window before heating it up.

2.7 Testing the Effect of the Windows on the Polarization of Light

As we want to find out, if the Fused Silica glass can be used instead of the N-BK7 glass, not only the vacuum has to be tested, but also the optical usability. Polarized light traveling trough the windows should change its polarization as little as possible.

The polarization of light is an important property, that describes the orientation of the oscillation of

electric field E. A light source is linear polarized, if the field only oscillates in one direction, and circular or elliptical polarized, if it circles around the wave vector k [34].

The polarization of fully polarized light with a phase ϕ can be described using the Jones vector [34]. The Jones vector can be explained by looking at the components E_x and E_y of complex amplitude of the electric field in x and y direction of light moving in z direction

$$E = \begin{pmatrix} E_x \\ E_y \end{pmatrix} = \begin{pmatrix} E_{0x} e^{i\phi_x} \\ E_{0y} e^{i\phi_y} \end{pmatrix}. \tag{2.1}$$

The Jones vector

$$J = \begin{pmatrix} E_{0x} e^{i\phi_x} \\ E_{0y} e^{i\phi_y} \end{pmatrix} \tag{2.2}$$

then characterizes the (relative) amplitude and phase of the components. E.g. for linear light in the x direction with $E_{0y} = 0$, one gets the Jones vector $\begin{pmatrix} 1 \\ 0 \end{pmatrix}$.

Since in reality most light is not linear polarized in one direction, but also in polarized in different directions, the Jones vector can be modified to $\begin{pmatrix} 1-\epsilon \\ \epsilon \end{pmatrix}$, where ϵ is the polarization orthogonal to the wanted polarization. A measure of the quality of linear polarized light is its extinction ratio (ER) given by the following formula

$$ER = \frac{\epsilon^2}{(1-\epsilon)^2} \approx \epsilon^2 \tag{2.3}$$

$$= \frac{T_{min}}{T_{max}}. \tag{2.4}$$

Here T_{min} and T_{max} are the minimal and maximal transmission of the light after going through a polarizer.

In Section 2.6 the rainbow pattern on both windows of the cell implies that the gluing process introduced stress to the windows. Stress on optical materials can lead to birefringence, which causes double refraction of the light passing through the material. That means that the ordinary ray (polarization component perpendicular to the optic axis, called p polarization) and the extraordinary ray (polarization component parallel to the optic axis, called s polarization) are refracted in different directions in the material [35]. Passing through such a material the ER of the light gets bigger, which is unwanted.

To measure the ER the construction in Fig. 2.18 was used. The apertures were used to align the beam straight over a line of holes onto the power head of the power meter. This was done with the outcoupler and the mirror by beam walking. The light coming out of the outcoupler is 780 nm laser light and supposed to be linear, the first polarizer filters out any unwanted polarization to make sure of that. With the second polarizer the minimal and maximal transmission gets set. The holder in Fig. 2.18(a) is padded with optics tissue to make sure the windows do not touch anything impure.

The ER of the windows were measured before the cell was glued. The ER of the cell was measured after the gluing of the windows, as well as after the second baking process. The ERs can be found in

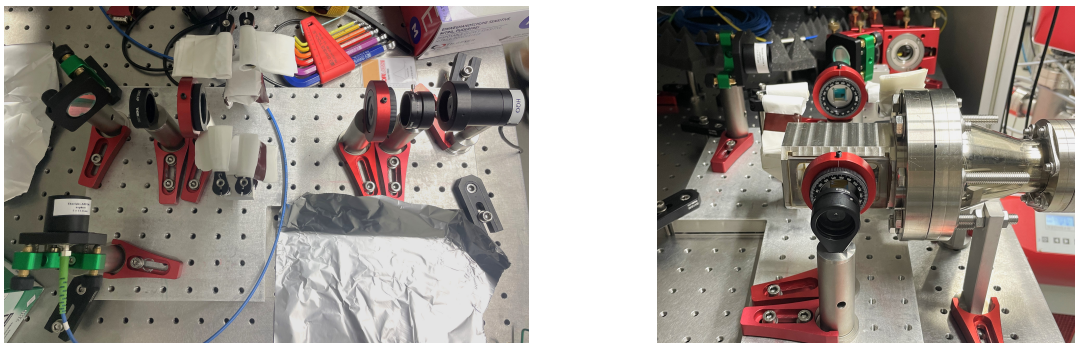

(a) construction with holder for windows

(b) construction with cell

Figure 2.18: Construction for measuring the ER of the used light.

Table 2.3. The errors on the minimum and maximum of transmission come from the inaccuracy of the power meter and the error on the ERs can be calculated using gaussian error propagation.

Table 2.3: ER of the light going trough the windows and the test cell

	T_{min}	T_{max}	ER
left window	$(0.010 \pm 0.005)\,\mu W$	$(1.980 \pm 0.005)\,mW$	$(5.1 \pm 2.5) \cdot 10^{-6}$
right window	$(0.010 \pm 0.005)\,\mu W$	$(1.600 \pm 0.005)\,mW$	$(6.0 \pm 3.0) \cdot 10^{-6}$
cell after 1. time baking	$(14.10 \pm 0.05)\,\mu W$	$(1.410 \pm 0.005)\,mW$	$(10.000 \pm 0.050) \cdot 10^{-3}$
cell after 2. time baking	$(50.90 \pm 0.05)\,\mu W$	$(1.260 \pm 0.005)\,mW$	$(40.40 \pm 0.20) \cdot 10^{-3}$

In Table 2.3 it can be seen, that the ER got up to four orders bigger after baking the cell. After baking it a second time it got a little bit worse, but not much. The ER of one single window after the second baking process should be around ER $\approx \frac{1}{50}$, as the ER add up for two windows.

2.8 Conclusion

In this chapter a vacuum cell with a titanium frame and fused silica windows could successfully be build. During the gluing process important informations for alternations to the process for future cells were found. The pressure went down to $4.0 \cdot 10^{-9}$ mbar, which is the lowest the used pump can reach. Unfortunately birefringence was introduced to the windows during the heating up of the cell. In Section 4.1 a more in depth conclusion is drawn.

CHAPTER 3

Probe and Control Setup

In the next few sections it will be explained how a part of the setup for the Rydberg excitation was built and characterized. The setup was build in such a way, that the space surrounding the cell was simulated to make sure all optics can be be placed around the cell in the future. When setting those optics up, the polarization of the 780 nm light was altered to circular polarized light.

To characterize the beam after hitting the optics, the equations shown in Section 3.1 are needed. In Section 3.2 the planned setup with the needed optics and its constrains are explained. The used laser beams are traveling through polarization-maintaining fibers (PMFs), before entering the the setup. The procedure to align the polarization of a laser beam with one of the main axes of those fibers is shown in Section 3.3. Putting optics into the setup, one has to make sure that the shape of the beam and the position of the focus after the achromatic lens is not altered. Different techniques for setting up optics and the characterization of the focus after those optics can be found in Section 3.4. The procedure to produce circular light inside of the vacuum cell is explained in Section 3.5.

3.1 Gaussian Beam

Before staring to work with the laser beams mentioned in the next couple of sections, there are a few equations that are needed to describe a light beam. Those equations can then later be used to describe the quality of the laser beam after going through optics by fitting the equations to the shape of the beam. The lasers we are using can be characterised by the Gaussian beam model, since they come out of a single mode amplifier. In this model the electric field E along the propagation axis z of the beam is described by the *transverse electromagnetic mode* (TEM), which is a solution to the paraxial Helmholtz equation [36]

$$E(z,\rho) = A_0 \frac{w_0}{w(z)} e^{-(\rho/w(z))^2} e^{ik\rho^2/2R(z)} e^{i(kz-\eta(z))}. \tag{3.1}$$

Here ρ is the transversal coordinate and A_0 a constant amplitude. The radius $w(z)$ of the beam describes the radius at which the intensity drops to $1/e^2$ of its maximal value for different positions along the z-axis, whereas w_0 describes the radius at the focus for $z = 0$. The wave number is k, $R(z)$ the radius of the individual wave fronts and $\eta(z)$ the Gouy-phase, which is a result of the bigger curvature at the focus

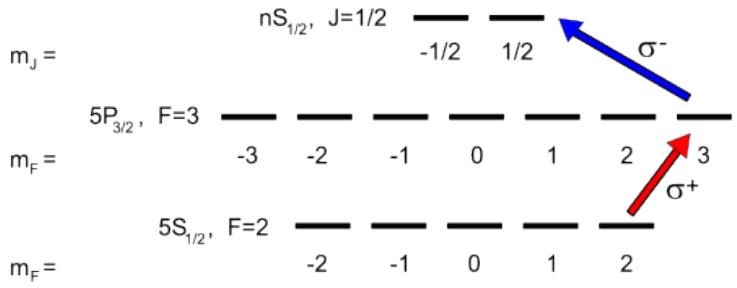

Figure 3.1: Ground, intermediate and Rydberg state of the Rubidium atoms with 780 nm laser with σ^+ polarization (red) and 480 nm laser with σ^- polarization (blue), which excite the atoms to the intermediate and Rydberg state.

as opposed to a plane wave. The waist w_0 at the focus can also be described by the Rayleigh range z_R

$$w_0^2 = \frac{\lambda z_R}{\pi}, \tag{3.2}$$

with λ being the wavelength of the light. The Rayleigh range is the distance, where $w(z) = \sqrt{2}w_0$. The beam changes most in a region of $-z_R \leq z \geq z_R$. Using the Rayleigh range, the waist $w(z)$ along the z-axis can then be written as

$$w^2(z) = w_0^2\left(1 + \left(\frac{z}{z_R}\right)^2\right). \tag{3.3}$$

The resulting intensity I of such a wave with an intensity I_0 at the origin $z = 0$, $\rho = 0$ is

$$I(z,\rho) = I_0\left(\frac{w_0}{w(z)}\right)^2 e^{-2\rho^2/w(z)^2}. \tag{3.4}$$

3.2 The Setup

As mentioned in Chapter 1 the setup for Rydberg excitation will be build around the vacuum chamber. Inside of the chamber are rubidium atoms. The scheme for the Rydberg excitation of those atoms can be seen in Fig. 3.1. At first the atoms are supposed to be in the $5^2S_{1/2}$, $F = 2$, $m_F = 2$ state [37]. Then the 780 nm σ^+ polarized laser, called probe laser, transfers it angular momentum to the atoms, which excites the atoms to the state with the largest corresponding angular momentum, which is the $5^2P_{3/2}$, $F = 3$, $m_F = 3$ intermediate state. From this state the atoms then get excited to the $n^2S_{1/2}$, $J = 1/2$, $m_j = 1/2$ Rydberg state with the 480 nm laser, called control laser.

For this excitation to work as well as possible, it is crucial that the probe laser has a pure σ^+ polarization. If there was also some σ^- polarization component, the $5^2P_{3/2}$, $F = 3$, $m_F = 1$ state would instead get excited with a small probability, see Fig. 3.2. This would reduce the coupling of the probe photons to the Rydberg state. It is particularly important to prevent that, if single photons should be coupled to Rydberg superatoms [38]. It would also lead to a system with more levels than three, which is harder to describe. Looking at Fig. 3.2, one can also see the Clebsch Gordan coefficients of the two transitions. The probability of a photon to couple to an atom is higher with bigger Clebsch Gordan coefficient.

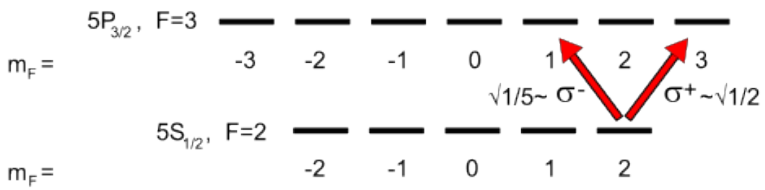

Figure 3.2: Ground and intermediate state of the Rubidium atoms with 780 nm laser with σ^+ and σ^- polarization, which excite the atoms to different states.

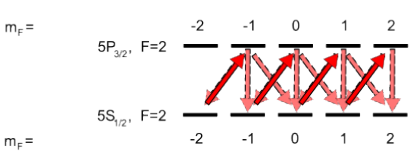

(a) Optical pumping with only σ^+ polarized light.

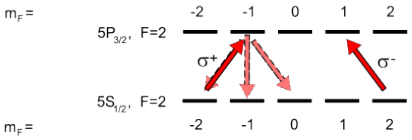

(b) optical pumping with σ^+ and σ^- polarized light, for better clarity only a few transitions are shown

Figure 3.3: Ground and intermediate states with 780 nm optical pumping laser (red) and decays (rosa).

That is why it is especially important for single photon experiments to have a clean σ^+ polarization, as it couples stronger to the atom. To create the right polarization for all laser beams, the half- and the quarter-wave plates (HWP and QWP) are used. With a HWP and a QWP one can create which ever polarization is needed inside of the cell, which will be shown in Section 3.5.

Another reason for optimal polarization is the outcome of the optical pumping. As mentioned before, the atoms should start in the $5^2S_{1/2}$, $F = 2$, $m_F = 2$ state for the 3 level scheme to work, but before the optical pumping the atoms could also be in any other m_F state. To ensure that only the $5^2S_{1/2}$, $F = 2$, $m_F = 2$ state is populated, the optical pumping with the 780 nm light is needed. The process of the optical pumping with pure σ^+ polarized light can be seen in Fig. 3.3(a). The σ^+ transition brings the electron to a $5^2P_{1/2}$, $F' = 2$ state with the value $m_{F'} = m_F + 1$. From there it can decay to a $5^2S_{1/2}$, $F = 2$ state with $m_F = \{m_{F'} - 1, m_{F'}, m_{F'} + 1\}$. After that the electrons get pumped again until they reach the highest m_F state. If there is now as well a σ^- polarized part of the light, the optical pumping will not work as well as before. That is because there are now also active transitions to smaller m_F values, which are not caused by decay, as seen in Fig. 3.3(b). The outcome can then be described by a rate equation. E.g. for light being equally divided into σ^+ and σ^- polarization, there will be equally many electrons in the $m_F = -2$ as in the $m_F = 2$ state.

In Fig. 3.4 the whole planned optical setup for the Rydberg excitation can be seen. The used parts are described in Table 3.1.

The lasers light comes out of the fiber couplers and travel through the optics, which functions are explained below, to the vacuum chamber.

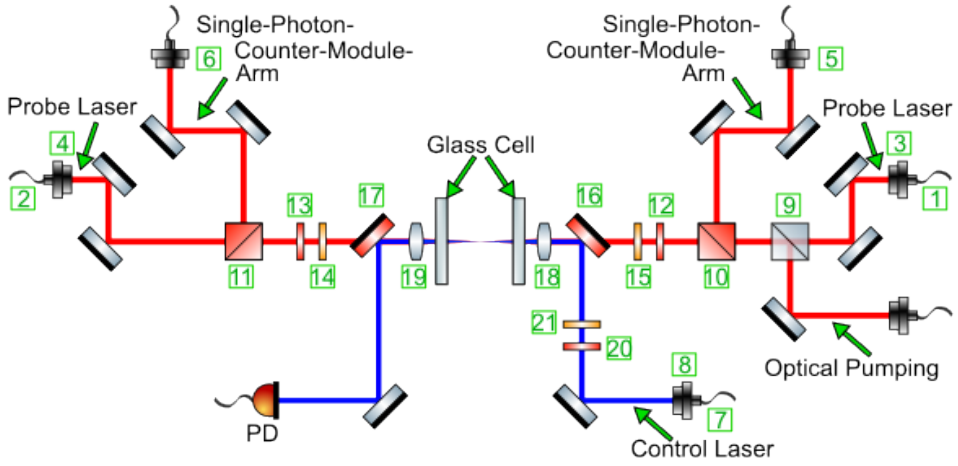

Figure 3.4: Planned optical setup for Rydberg excitation, the 780 nm probe laser is shown in red, 480 nm control laser is shown in blue, the numbers correspond with those of the optics parts described in Table 3.1.

Table 3.1: Optics, that are used in the Rydberg excitation setup with numbers corresponding to those in figure in Fig. 3.4.

number	part	description
1, 2	Thorlabs P3-780PM-FC-10	single mode fiber for 780 nm probe laser
3, 4	Thorlabs TC25APC-780	triple collimator to collimate 780 nm laser after fiber
5, 6	Thorlabs A110TM-B	aspheric lens (f = 6.24 mm) to couple 780 nm laser into fiber leading to a single-photon-counter-module (SPCM)
7	OZ Optics QPMJ-3AF3AF-488-3.5/125-3A-8-1	single mode fiber for 480 nm control laser
8	Thorlabs A220TM-A	aspheric lens (f = 11 mm) to collimate 480 nm laser after fiber
9	Thorlabs BS005	50:50 non-polarizing BS cube transmitting light from 700 nm to 1 100 nm to overlap optical pumping laser
10, 11	Thorlabs PBS12-780	PBS cube transmitting 780 nm light to split the light for the SPCM from the counter propagating probe laser
12, 13	Union Optic WPZ2312-780-M25.4	HWP coated for 780 nm light
14, 15	Union Optic WPZ4312-780-M25.4	QWP coated for 780 nm light
16, 17	Thorlabs DMLP650	dichroic mirror transmitting light over 650 nm to overlap 480 nm control laser
18, 19	Edmund Optics #49-331	achromat (f = 80 mm) to focus beams
20	Union Optic WPZ2320-480-M25.4	HWP coated for 480 nm light
21	Union Optic WPZ4312-480-M25.4	QWP coated for 480 nm light

The light for the optical pumping is brought into the setup by sending it onto a beam splitter (BS), which overlaps it with the probe beam. This is done before the HWP and the QWP such that the polarization optics can be used for both probe and the optical pumping beam, as they both need to be σ^+ polarized. For more information about the functionality of a BS see Appendix A.3.1.

After the BS, the light passes a polarizing beam splitter (PBS), which transmits p-polarized light and reflects s-polarized light. For more information about the functionality of a PBS see Appendix A.3.1 as well. The PBS is needed in that place to separate the probe laser beam going towards the cell from the counter propagating light. The light going towards the cell is transmitted by the PBS, but the counter propagating light, which is differently polarized, is reflected into a fiber, which directs the light to a single photon counter module (SPCM).

In front of the lens the probe beam gets overlapped with the 480 nm control laser by a dichroic mirror. The dichroic mirror reflects light with wavelengths below 650 nm and transmits light with wavelengths above that. For more information about the functionality of a dichroic mirror see Appendix A.3.2.

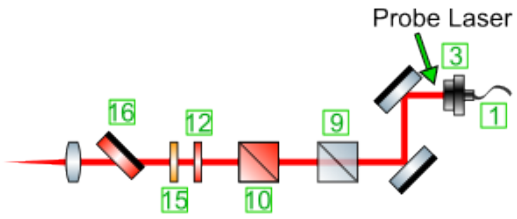

Figure 3.5: The part of the optical setup for Rydberg excitation, that was build in this thesis, the 780 nm probe laser is shown in red, the numbers correspond with those of the optics parts described in Table 3.1.

After the dichroic mirror the beams go through the lenses around the vacuum chamber. An achromatic lens was chosen, because achromatic lenses reduce chromatic aberrations and therefore help to prevent that the foci of the 780 nm and the 480 nm laser do not align because of these aberrations [34]. The lens does not ensure that the foci align, as there can still be astigmatism, because of oblique incidence of light or the optics in front of the lens introducing aberrations, as seen in Section 3.4. One could also use an aspherical lens to help remove aberrations, but they are really hard to align, which is why the achromatic lenses will be used. The probe laser has to have a waist at the focus of $w_0 \lesssim 10\,\mu\text{m}$ for Rydberg blockade interactions to happen between the Rubidium atoms [3]. The control beam has to have a bigger waist at the focus, such that all atoms excited to the intermediate state can interact with the control beam. This helps to prevent losses of atoms, which are already in intermediate states. It is also done to obtain a more uniform Rabi frequency across the atom cloud. But the foci of both beams can also not be arbitrary small below those 10 µm, as the interactions are supposed to happen above a chip with an oscillator on it. The foci getting smaller leads to a faster rise in divergence and as a result the beams would get cut by the oscillator, as shown in Samuel Germer's bachelor thesis [12]. The waist has to stay above $w_0 = 5\,\mu\text{m}$. One has also to take into account that the lenses are standing outside of the cell and that the cell has a certain length. That is why the focal length of the lenses have to be bigger than $f = 50\,\text{mm}$. In Samuel Germer's bachelor thesis different combinations and their waist diameters are shown, but in the end one settled for the following combinations. The lenses infront of the cell have a focal length of $f = 80\,\text{mm}$ and together with the collimators after the probe laser outcouplers, which have a focal length of $f = 25.08\,\text{mm}$ and collimate the probe beams after the fibers, it creates a theoretical focus of $w_0 = 7.98\,\mu\text{m}$. In combination with the collimator after the control laser outcoupler, which has a focal length of $f = 11\,\text{mm}$, the lens creates a waist of $w_0 = 12.72\,\mu\text{m}$. Those waist diameters meet the mentioned constrains and have already been tested in Samuel Germer's bachelor thesis.

In this chapter the part of the setup shown in Fig. 3.5 was build.

3.3 Polarization-maintaining Fiber

As explained in Section 3.2 the probe beam has to be σ^+ polarized in the cell and the polarization is set with the HWP and QWP, but before that the light we are working with is horizontally polarized. The well defined polarization even before the cell is needed, as the optics are often differently coated for horizontal or vertical light. As the light has to go through fibers to move it over longer distances

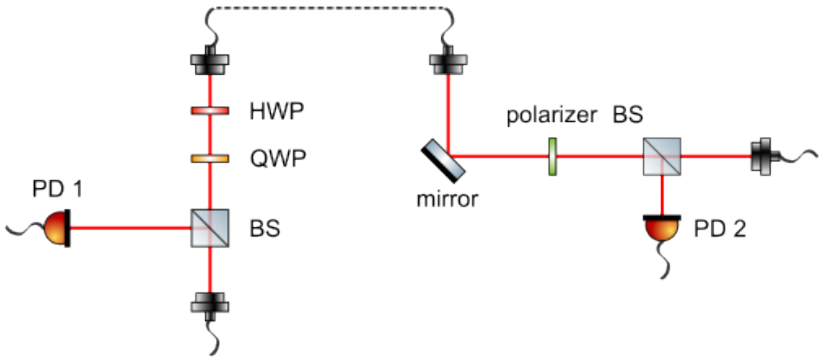

Figure 3.6: The setup to align the polarization of the 780 nm laser with one of the main axis of a PMF.

without interfering with other constructions, we want to make sure that the polarization of the light gets maintained. That is why we are using polarization-maintaining fibers.

Non-polarization-maintaining fibers have a round symmetry, therefore two polarization modes are travelling with the same speed through the fiber [39]. If there is now a disturbance because the fiber got bend or there was a temperature change, birefringence is induced. The polarization at the end of the fiber varies with bending, temperature and even change of frequency. In polarization-maintaining and absorption-reducing (PANDA) fibers to prevent that the birefringence messes up the polarization, a birefringence gets introduced in a controlled way by putting two stress rods into the cladding. The stress rods create a slow and a fast axis, as the two mode velocities differ. If the incoming light is aligned with one of the induced axes, disturbances are cancelled.

To make sure the polarization is aligned with one of the main axes, the construction in Fig. 3.6 was used. The fiber should be put into the coupler in such a way that one of the main axes is perpendicular to the optical table to easily match the polarization to it. With the half-wave plate (HWP) the polarization can be rotated to meet this axis. The quarter-wave plate (QWP) in front of the HWP can be used to compensate any unwanted elliptical polarization of the incoming laser light, as well as elliptical polarization that might occur because the fiber is glued into the connector, which can induce stress birefringence. After the fiber the light gets directed through a polarizer. The intensity of the light behind that polarizer alters, if the polarization of the incoming light changes or, more explicitly, if the main axis is not met. The two 50/50 beam splitters (BSs) exist to guide a part of the light in front of the construction onto a first photodiode (PD) and a part of the light after the polarizer onto a second PD.

The output of the two PDs can than be watched on an oscilloscope. The math mode of the oscilloscope is used to generate the quotient of the two signals. To check, if the axis is met, a disturbance gets introduced by scanning the frequency of the laser without any mode hopping. The signals, that can be observed, are shown in Fig. 3.7. The blue signal is the signal of the laser scan, the yellow signal is the signal of the PD before the fiber, the green signal is the signal of the PD after the fiber and the red signal is the quotient of the signals of the two PD's. The polarization is aligned with one of the axes of the fiber, when the signals of the PD's are proportional even tough the laser scan introduces a disturbance. That means the quotient should be close to a straight line, when the polarization is aligned. If it is not aligned, the quotient will oscillate.

To align the polarization with the main axis, the polarizer gets rotated until the slope of the quotient is

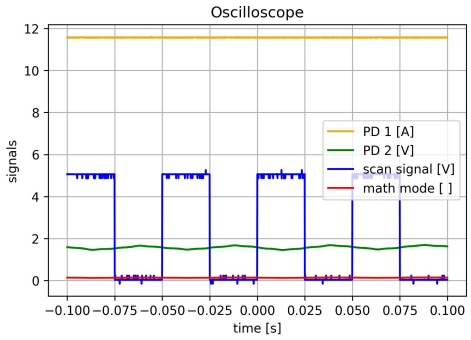

Figure 3.7: Oscilloscope picture of input polarisation being off; Green: PD after fiber. Yellow: PD before fiber. Blue: Laser scan trigger. Red: Math function: Green/Yellow

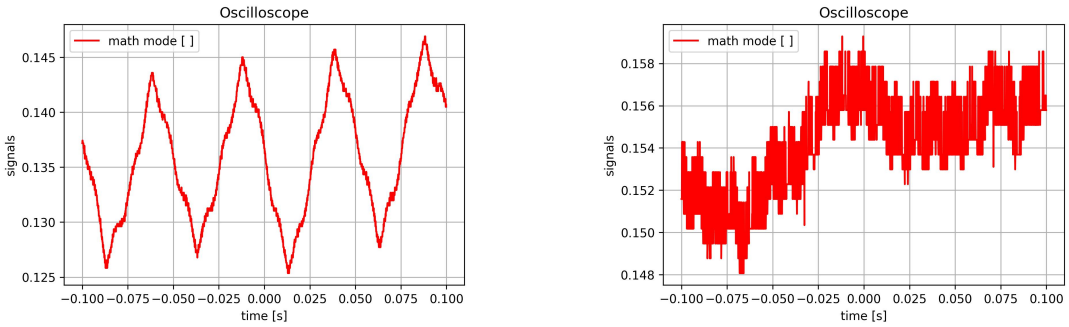

(a) not meeting one of the main axes of the fiber

(b) meeting one of the main axes of the fiber

Figure 3.8: Quotient of signals of first and second PD, input polarization does or does not meet one of the main axes of the fiber.

maximal. Then the slope gets flattened by slightly rotating the HWP and the QWP. Theses two steps get repeated, until the slope is minimal (see Fig. 3.8(b)) and even minimal changes below 1° lead to big changes in the slope. Another evidence that the main axis is met, is that the slope changes its sign. The alignment can now be tested on its resistance against disturbances by moving the fiber. Additionally, one should make sure, that the slope does not change over a period of at least half an hour. If the slope is steady the ER after the polarizer can be measured. We got $T_{min} = (0.115 \pm 0.005)\,\mu W$ and $T_{max} = (52.4 \pm 1.0)\,\mu W$ and therefore $ER = (2.20 \pm 0.10) \cdot 10^{-3}$. After this procedure the polarizer and the BSs can be taken out of the setup.

3.4 Setting up Optics without Changing Shape and Focus of Probe Laser

Now that the light's polarization gets maintained throughout the fiber, the actual optics can be set up. The set up was already partly build by Samuel Germer with some important optics missing and without the consideration of space constrains [12]. After aligning the lens, as it is also described in Samuel Germer's bachelor thesis, the BS, PBS, HWP, QWP and dichroic mirror are supposed to be put into the

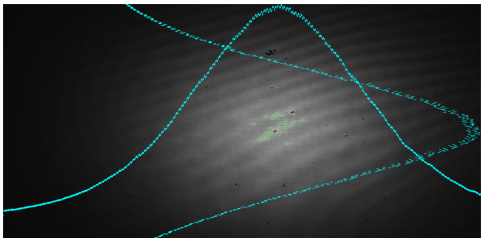

Figure 3.9: position of beam on the arducam without PBS

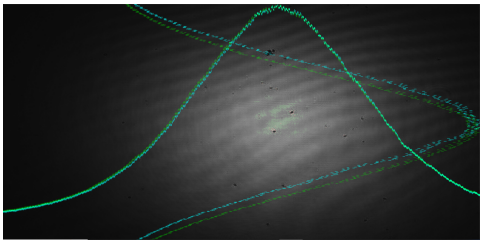

(a) not corrected position

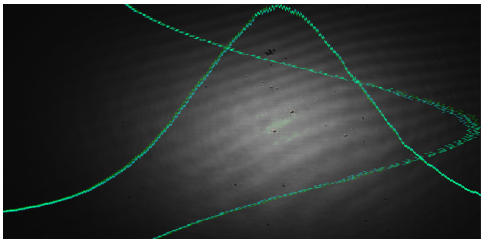

(b) corrected position

Figure 3.10: Position of beam on the arducam without PBS (green) and with PBS (blue).

setup without disturbing the laser beam.

The optics can be aligned by using the Arducam MT9J001 with the Arducam Beam Profiler software, which was developed by Samuel Germer. The Arducam can be placed with a distance of $2f$ from the lens to observe the position of the beam hitting the lens. This works because at a distance of $2f$ the picture is reversed, but has the same size as the light at the position of the lens [34]. As the alignment process with the arducam is the same for all optics, it is exemplary shown for the PBS. Fig. 3.9 shows the position of the beam before placing the PBS. This picture can be hold in the program by pressing the key H. Now the PBS gets put into the setup. The saved picture without the PBS then gets overlayed with the current picture with the PBS and the position of the PBS can be altered until the horizontal beam profiles overlap perfectly (see Fig. 3.10(a)). But one can also see in Fig. 3.10(a) that the vertical position of the beam moved as well. This can be corrected with the second mirror after the fiber. The position of the beam can be moved, until both pictures overlap completely (see Fig. 3.10(b)).

This was done for all optics except the dichroic mirror. As seen in Appendix A.3.2 the dichroic mirror introduces a beam offset. This makes the positioning of the dichroic harder than the positioning of the other optics. That is why the mirror got put into the setup before placing any other optics. As the mirror was put into the setup before placing the lens, it was aligned trough two apertures instead of placing it with the arducam.

The BS, PBS and dichroic mirror have not only to be placed in a way such that they do not disturb the probe laser, but also such that the additional laser beams are hitting them in the middle and not oblique. To do so a laser pointer was used to simulate the light of the optical pumping, the SPCM and the control laser arm, as seen in Fig. 3.11 for the PBS. With the laser pointer it could be made sure, that a laser going straight over a line of holes on the optical table hits the PBS in the middle and leaves it in a 90° angle.

In Section 3.1 it was explained that the beam of the 780 nm probe laser meets the requirements of a

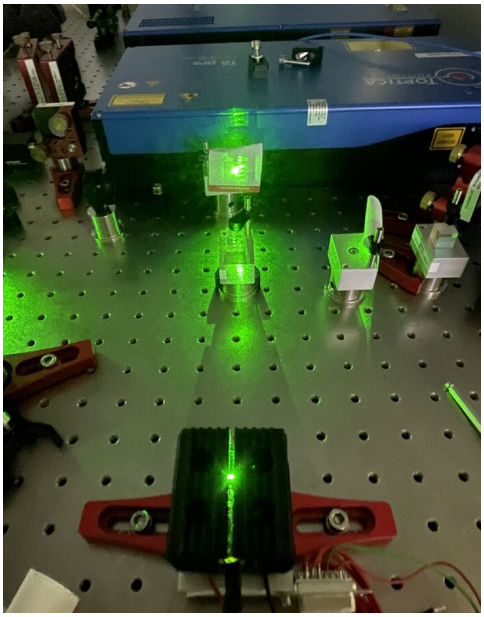

Figure 3.11: Laser pointer for aligning PBS for the single photon counter module.

Gaussian beam. Every optics the laser beam has to pass through is potentially changing its shape, which is why the shape of the beam has to be inspected every time a new optic is put into the setup. After aligning the optic with the arducam, a picture of the beam and the background is taken. To get rid of any background radiation, that may distort the beam profile, the entries of the background pictures get subtracted from the beam picture. The intensity in vertical and horizontal direction can be determined by summing the resulting entries for the vertical axes and the entries for the horizontal axes. To examine if the beam can still be described by the Gaussian beam model after traveling through an optical component, the next shown Gaussian function Eq. (3.5) following the exponential part of Eq. (3.4), with f being the factors in front of the exponential part, is fitted onto the data of the vertical and horizontal intensity profiles with the same routine, that was used by Samuel Germer [12]

$$I(z,\rho) \propto f e^{-2(\rho-\rho_0)/w(z)^2}. \tag{3.5}$$

In Fig. 3.12 the intensity profiles with the Gaussian function fits and the residues of the data to the fits can be seen for all optics that were placed into the setup. The values of the fitted Gaussian curves and their errors can be found in Tables A.3 and A.4 and in Tables A.5 and A.6, where the pixels were converted to µm by multiplying with the pixel size 1.67 µm.[1] When studying the residuals of the fits in Fig. 3.12, one can see, that the data of the vertical beam differ from the Gaussian fit. This is because of an interference pattern that is caused by the glass plate in front of the pixels and was already seen in the Bachelor thesis of Samuel Germer [12]. If one takes that into account, the Gaussian fits are still good.

As explained in Section 3.2 there is not only a constrain for the shape of the beam but also for the

[1] Above it was described that the dichroic mirror was put into the setup before the lens was placed, as a consequence it was not aligned with the arducam. That is why the pictures for beam profile of the dichroic mirror were taken after placing the lens.

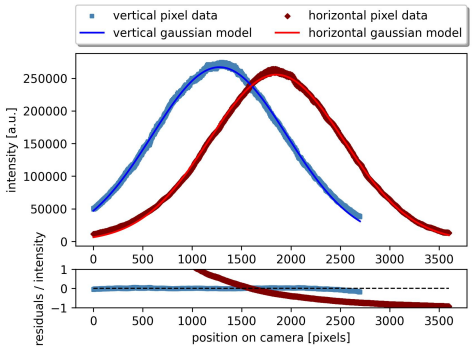

(a) after placing the dichroic mirror

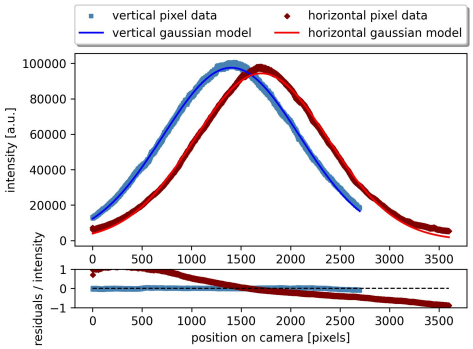

(b) after placing the BS

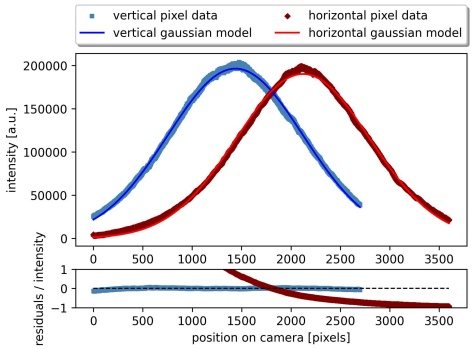

(c) after placing the PBS

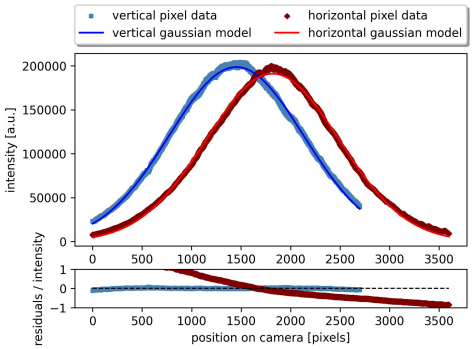

(d) after placing the HWP

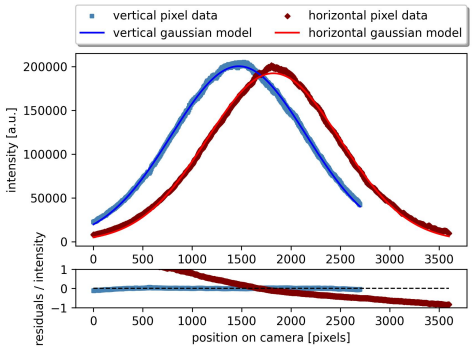

(e) after placing the QWP

Figure 3.12: Horizontal and vertical intensity profile of the beam at $2f$ behind the lens with Gaussian fits and the residuals of the intensity data to those fits.

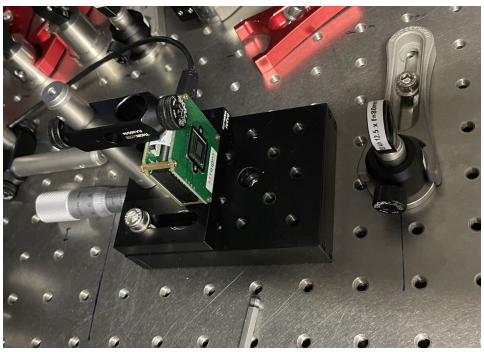

Figure 3.13: Arducam on a translation stage to take pictures around the focus

focus after the lens. The 780 nm probe laser has to be focused such that $w_0 \approx 8\,\mu m$ [12]. But the focus after the lens can be changed by the optics as well if they are not placed well enough. To make sure the constrains are still met, the focus has to be determined when placing an optic. To do so the arducam was mounted onto a translation stage, which is roughly placed where the focus should be, as seen in Fig. 3.13. The beam can then be observed in the program of the ardcam. With the translation stage the arducam can be moved along the beam around the position of the focus. Pictures of the beam and the background can be taken in evenly distributed intervals along a distance from about $w_0 - z_R$ to $w_0 + z_R$. In the same way as described earlier in this chapter, the beam profiles and Gaussian curve fits are calculated for these pictures. The radii $w(z)$ can then be plotted against their position z on the z-axis. By fitting the next shown equation in Eq. (3.6) following Eq. (3.3) to these dates, the radius w_0 at the focus can be calculated, using

$$w(z) = w_0 \sqrt{\left(1 + \left(\frac{z - z_0}{z_R}\right)^2\right)}. \tag{3.6}$$

The fits for the focus for the horizontal and vertical axis after every optic can be seen in Fig. 3.14 and the values of the parameters of the fits can be seen in Tables A.7 and A.8. It can be noted that even though the radii w_0 of the focus stay below 10 nm for the horizontal and vertical axis, the foci of the two axes are not at the same position on the z-axis.

There could be multiple reason for this astigmatism. An easy explanation could be, that the beam coming out of the fiber is collimated differently on both axes. But taking a look at the horizontal and vertical radius of the beam over a distance of 1 m in Fig. 3.15, this seems not to be the case. The radius of the vertical axis grows by approximately 25 µm over 1 m and the one of the horizontal only by 10 µm. The radii were again calculated by fitting Eq. (3.5) to the beam profiles in python and then Eq. (3.6) was fitted to those radii. The fit parameters can be seen in Table 3.2. This collimation is sufficient,

Table 3.2: Values of fit variables for Eq. (3.6) for collimation measurement.

	w_0 in µm	z_0 in µm
vertical	$2\,265.5 \pm 7.5$	$(45.0 \pm 3.5) \cdot 10^{-5}$
horizontal	$2\,251.0 \pm 2.0$	$(15.0 \pm 3.0) \cdot 10^{-5}$

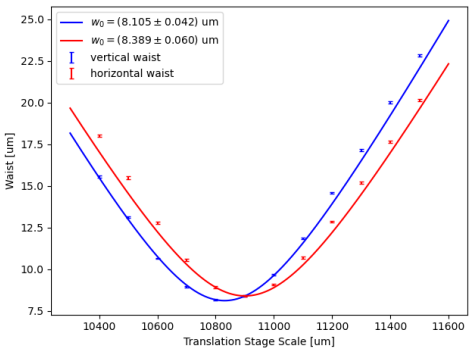

(a) after placing the dichroic mirror

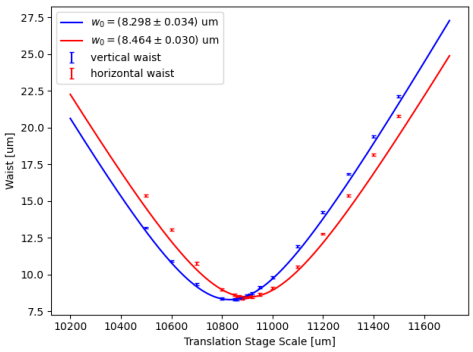

(b) after placing the BS

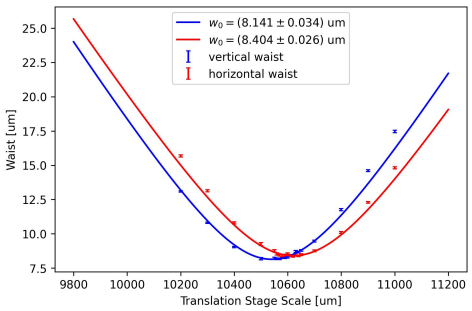

(c) after placing the PBS

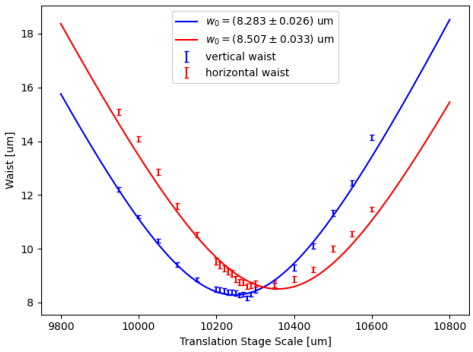

(d) after placing the HWP and QWP

Figure 3.14: Horizontal and vertical radii $w(z)$ along the z-axis and fits to the data points with residues

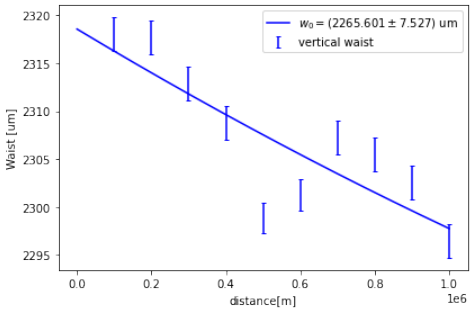

(a) vertical

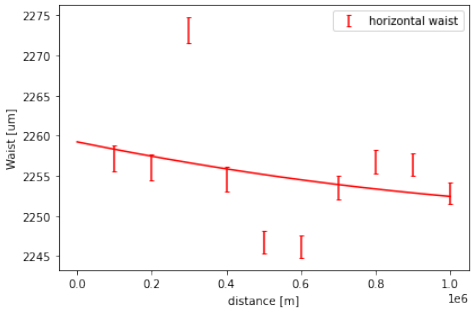

(b) horizontal

Figure 3.15: Horizontal and vertical radii $w(z)$ along the z-axis over a distance of 1 m with no optics.

when comparing it with the collimation Samuel Germer measured for the same fiber and collimator [12]. Another possibility is that the lens or one of the other optics are positioned at an angle. The astigmatism can already be seen in the first picture after placing the lens infront of the dichroic mirror, additionally the position of every optic apart from the dichroic mirror was examined with the arducam. That indicates that the mirror or the lens possibly induce the astigmatism. To test if this astigmatism is induced by the lens, the position of the lens was supposed to be altered. To do so the lens was put in the newly build lens mount, which can be seen in Fig. 3.16. This lens mount is needed to bring the lens as close as possible

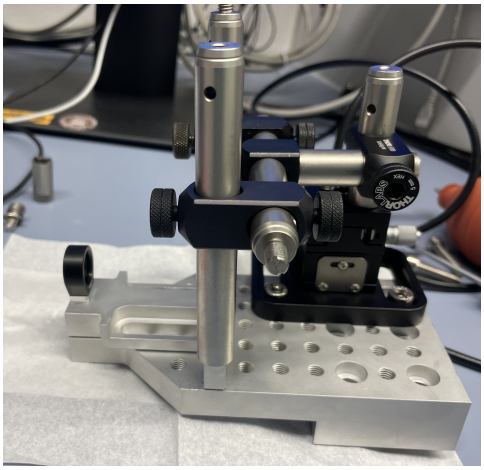

Figure 3.16: New lens mount, the upper plate with the lens can be moved by the translation stage.

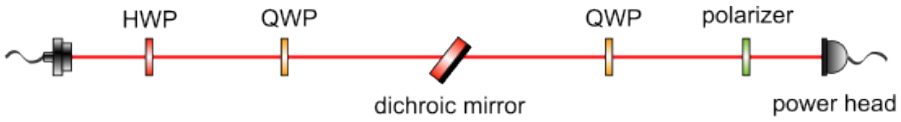

Figure 3.17: Simplified setup to create circular light, light travels from the left to the right passing trough a HWP, a QWP, the dichroic mirror and the reference construction consisting of a QWP and polarizer before hitting the power head.

to the cell. The lens can be moved by a translation stage moving the plate, the lens is placed on. The height of the lens is set with thin plates, that can be placed beneath it. Unfortunately after building the lens mount, there was not time left to investigate the astigmatism further.

3.5 Production of Circular Light

Inside of the vacuum cell the light is supposed to be circular. The polarization is linear until the light hits the dichroic mirror. The dichroic mirror, the lens and the window of the cell alter the polarization. The simplified setup in Fig. 3.17 can be used to create circular light. The HWP and QWP are used to alter the polarization. The QWP and the polarizer on the right side of the dichroic mirror form a reference construction, as they are set in such a way, that the intensity of the light hitting the power head is either minimal or maximal for circular light passing through the construction. Normally for linear polarized light one would only need a QWP to change it to circular polarized light, but the dichroic mirror induces an unknown alternation of the polarization. Therefore an additional HWP is needed to alter the polarization to any possible polarization.

To better visualize what the individual components do to the polarization, the Poincaré sphere can be

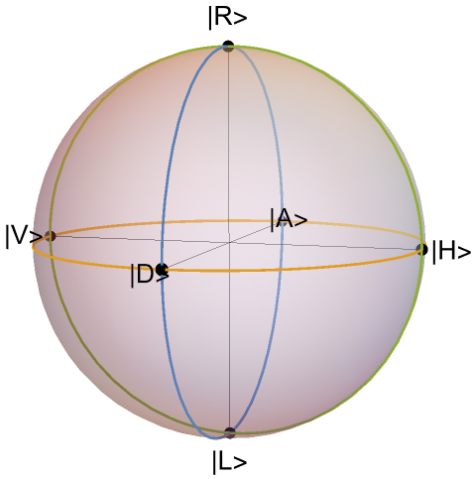

Figure 3.18: The Poincaré sphere to visualize the polarisation light; the north and south pole represent right R and left L hand circular polarized light, H and V represent horizontal and vertical polarization, D and A represent diagonal and anti-diagonal light.

used, which can be seen in Fig. 3.18. The sphere was programmed in Mathematica. The program was previously developed by our group and altered by me. On the sphere each point represents a possible polarization [40]. In this representation the north pole corresponds to right hand circular polarized light R and the south pole to left hand circular light L. On the equator the horizontal polarization H is opposite the vertical polarization V. The other points on the equator correspond to linear polarizations with D being diagonal and A being antidiagonal light. The remaining points on the sphere correspond to elliptical polarization. A point on the sphere can now be described by its longitude $-180^\circ \leq 2\lambda \leq 180^\circ$, measured clockwise starting at H for positive values, and its latitude $-90^\circ \leq 2\lambda \leq 90^\circ$, measured upward from the equator for positive values. The polarization of an arbitrary point is equivalent to elliptical polarization with an azimuth λ seen from the horizontal and an ellipticity of $\tan|\omega|$.

In Fig. 3.19 the poincaré spheres, which were programmed in Mathematica, for a HWP, QWP and a polarizer can be seen. The polarization of the input light, shown as a green vector, can be changed to any point on the dotted path by rotating the respective waveplate or polarizer. When looking at Fig. 3.19(c), one can see, that the purple dotted path is mostly not on the surface of the poincaré sphere. Polarization is normally only defined on the surface of the poincaré sphere. But to indicate, that the polarizer does not only change the polarization, but also changes the intensity of the light passing trough, the length of the purple vector, also called norm, was programmed to be proportional to the intensity of the light after the polarizer.

An example for horizontally polarized light traveling trough a HWP and changing its polarization can be seen in Fig. 3.20. The green vector represents the incoming horizontal polarized light and the blue vector represents the outgoing light. Depending on the rotation of the waveplate a different polarization of the outgoing light can be reached. If the horizontal light goes trough a HWP, which is rotated by 0°, it stays horizontal, but if it hits a HWP, that is rotated by 90°, it becomes vertical.

An example for the effect of the reference construction, consisting of a QWP and a polarizer, as seen in Fig. 3.17, on incoming right hand polarized light can be seen in Fig. 3.21. Incoming right hand circular

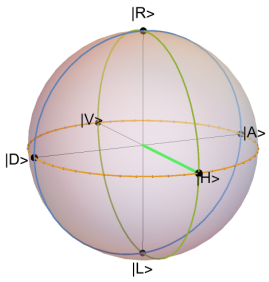

(a) HWP, possible polarisations of outgoing light blue dotted

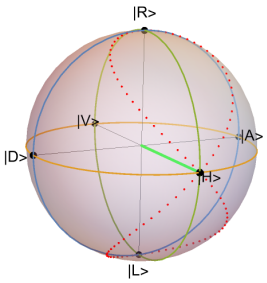

(b) QWP, possible polarisations of outgoing light red dotted

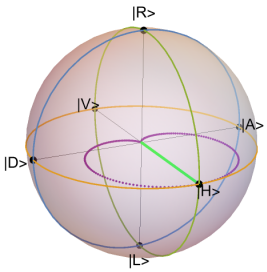

(c) polarizer, possible polarisations of outgoing light purple dotted

Figure 3.19: The poincaré spheres for incoming horizontal polarized light (green vector) going through a HWP (blue dotted), a QWP (red dotted) and a polarizer (purple dotted), the dotted paths represent the possible polarizations of the outgoing light.

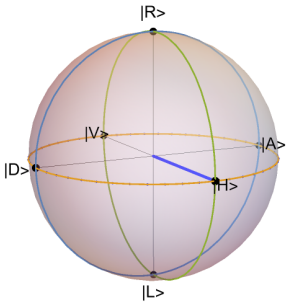

(a) HWP rotated by 0°, outgoing light (blue vector) is still horizontal polarized

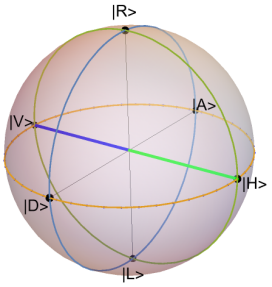

(b) HWP rotated by 90°, outgoing light (blue vector) is now vertical polarized

Figure 3.20: Incoming horizontally polarized light (green vector) changing its polarization (blue vector), when going through a HWP rotated by 0° or 90°.

light, represented by the yellow vector, travels trough the QWP and becomes linear (orange vector). The polarizer after the QWP can then turn the polarization to any point of the purple dotted path. It is rotated in such a way that it is perpendicular to the QWP. That leads to the intensity and therefore the norm of the purple vector getting minimal for right hand circular light. That is why the purple vector can not be seen, as its length is to small. For every other incoming polarization the intensity does not get minimal and the norm of then purple vector is norm ≥ 0.

Now the effect of all components, shown in Fig. 3.17, on the linear polarization of the incoming light of the experiment and the iteration process to get to circular polarized light can be studied. In the following example the starting polarization of the incoming light is horizontal (green vector) and the outgoing light (purple vector) is supposed to be shifted to right-hand circular polarized light. The polarizations of the light after going through an optic are again represented by differently colored vectors: blue - after HWP, red - after QWP, yellow - after dichroic mirror, orange - after second QWP, purple - after polarizer. For clarity the vectors were also divided into two poincaré spheres. The left one always represents the light on the left side of the dichroic mirror and the right one represents the light on the right side of the dichroic mirror. Here left and right side refer to the construction in Fig. 3.17. To give a

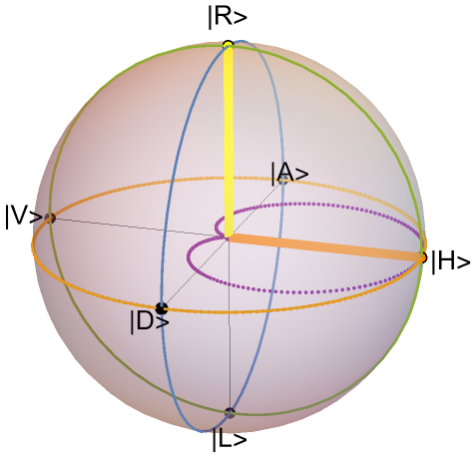

Figure 3.21: The poincaré sphere of incoming right hand circular polarized light (yellow) going through the QWP (orange) and then the polarizer (purple) of the reference structure (the purple vector can not be seen, as its norm represents the intensity of the light after the polarizer and that is minimal for the incoming horizontal light after the QWP).

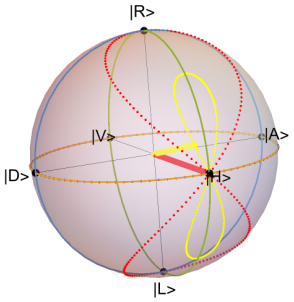

(a) Incoming horizontal light (green) going trough non-rotated HWP (blue), non-rotated QWP (red) and then the optics with an unknown polarization (yellow), green and blue vector can not be seen, as they are under the red vector.

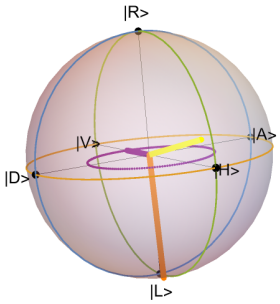

(b) Light after the optics, that shift light to an unknown polarization, (yellow) going through the QWP (orange) and the polarizer (purple) of the reference structure.

Figure 3.22: Beginning of the optimization procedure: incoming horizontal light (green) going through the whole polarization construction, norm of outgoing light (purple) is norm = 0.625097, vectors are split into two spheres for better identification.

reference point, the light after the dichroic mirror, represented by the yellow vector, is shown in both poincaré spheres.

The starting position for this example can be seen in Fig. 3.22. As mentioned before, in this example the light is horizontally polarized (green vector) in the beginning. The first HWP can now move the polarization to any point on the blue dotted path, but at the beginning it should be placed such that it does not alter the polarization. Thus the polarization after the HWP (blue vector) is still horizontal. Likewise the QWP can shift the polarization to any point on the red dotted path, but will also at the start be rotated such that it does not alter the polarization. The polarization after the QWP (red vector) is still horizontal. After the HWP and the QWP the light passes the dichroic mirror, the lens and the

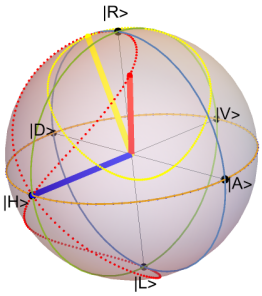

(a) Incoming horizontal light (green) going trough non-rotated HWP (blue), a rotated QWP (red) and then the optics with an unknown polarization (yellow), green vector can not be seen, as it is under the blue vector.

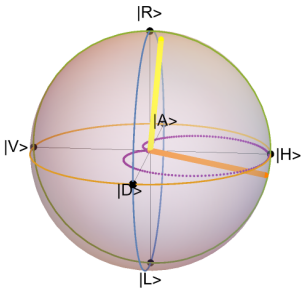

(b) Light after the optics, that shift light to an unknown polarization, (yellow) going through QWP (orange) and polarizer (purple) of the reference structure.

Figure 3.23: First step of the optimization procedure: incoming horizontal light (green) going through the whole polarization construction, norm of outgoing light (purple) is norm = 0.127777, vectors are split into two spheres for better identification.

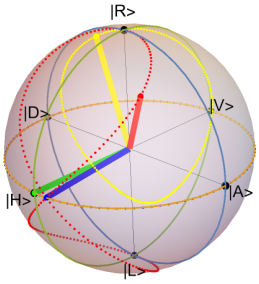

(a) Incoming horizontal light (green) going trough a rotated HWP (blue), a rotated QWP (red) and then the optics with an unknown polarization (yellow).

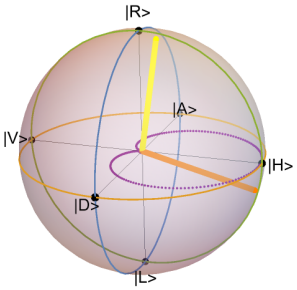

(b) Light after the optics, that shift light to an unknown polarization, (yellow) going through QWP (orange) and polarizer (purple) of the reference structure.

Figure 3.24: Second step of the optimization procedure: incoming horizontal light (green) going through the whole polarization construction, norm of outgoing light (purple) is norm = 0.109965, split into two spheres for better identification.

(a) Incoming horizontal light (green) going trough rotated HWP (blue), rotated QWP (red) and then the optics with an unknown polarization (yellow).

(b) Light after the optics, that shift light to an unknown polarization, (yellow) going through QWP (orange) and polarizer (purple) of the reference structure.

Figure 3.25: Final step of the optimization procedure: incoming horizontal light (green) going through the whole polarization construction, norm of outgoing light (purple) is norm = 0, split into two spheres for better identification.

window, which introduce an unknown polarization shift (yellow vector). The polarization is now at the point where the yellow vector is pointing at. The light then travels through the QWP (orange vector) and the polarizer (purple vector) from the reference construction and ends at the purple vector, seen in Fig. 3.22(b). The norm of the purple vector can be calculated and is proportional to the intensity of the light after the polarizer. In the real experiment this intensity is the only thing one can actually observe with a power meter. In the beginning the norm is norm = 0.625097 for this example.

The iteration process then gets started by rotating the QWP until the norm of the purple vector gets minimal, see Fig. 3.23. The norm of the purple vector is now norm = 0.127777 and therefore already so small, that it can not be seen anymore, but the yellow vector indicates, that the right hand circular polarization is still not met.

After that the QWP gets turned until the intensity gets even smaller, see Fig. 3.24. The norm is now at norm = 0.109965. These two iteration steps get repeated until the norm of the purple vector is zero and the end polarization therefore right hand circular, see Fig. 3.25.

As mentioned before, in the real experiment only the intensity after the polarizer can be measured, but the iteration steps are still the same step as explained above. To really make sure the circular polarization is reached, the polarizer can be fully rotated, while the intensity is being watched. If the intensity after the polarizer does not noticeably change, the light inside of the cell is circular.

3.6 Conclusion and Outlook

In this chapter the polarizatio of the 780 nm laser could be set really well. After setting up the optics the 780 nm laser could still be focused to $\approx 8\,\mu$m, but the foci for the horizontal and vertical axis are not at the same point, which has to be corrected in the future. In Section 4.2 a more in depth conclusion is drawn.

CHAPTER 4

Conclusion

4.1 Self-build Titanium-Fused-Silica-Test-Cell

Regarding the tightness of the test cell the outcome is very positive. There was one leak at one of the windows, but it could easily be fixed with the "330-VACSEAL-S". And after the second baking process the dominant peak in the mass spectrum, which limits the pressure, belonged to H_2O, which indicates that there are no further leaks on this scale.

Over the time of one week the pressure inside the cell went down to $4.0 \cdot 10^{-9}$ mbar. For cold atom experiments an UHV with a pressure of at least 10^{-8} mbar is needed. But for some experiments a pressure of up to 10^{-12} mbar is needed, as the lifetime of atoms in a magneto-optical-trap is getting shorter the more background collision are happening [9]. This background collisions are rising with the pressure. E.g. for some Bose-Einstein condensates (BECs), that get cooled with evaporative cooling and are therefore already loosing atoms because of that, the lifetime of the atoms has to be up to a few minutes, which is why such low pressures of 10^{-12} mbar are needed [41, 42]. The pressure in this cell is still too high for those experiments. To test, if the cell could be used for BEC experiments an ion pump would be needed, as the power pump has reached its limit and the cell would need to be heated up again. Therefore one might not be able to say, if the vacuum of the cell can be used for BEC experiment, but it is definitely sufficient for other cold atom experiments.

But unfortunately the outcome for the optical part is not that positive. The ER for the cell after the second baking process is ER = $(40.40 \pm 0.20) \cdot 10^{-3} \approx \frac{1}{25}$. The ER for one single window should be around ER $\approx \frac{1}{50}$. The ER for normal optics, e.g. fibers, is ER $\approx \frac{1}{100}$, which is two times better than the ER of the cell. This is not good, but for birefringence, that causes a constant phase shift, this can still be compensated with polarisation optics, as seen in Section 3.5. Therefore the cell could be used with polarization optics for small beam sizes, but for bigger beam sizes the birefringence may be hard to compensate, because of changes of the birefringence in the extent of the beam. To improve the ER in the future the size and the form of the windows could be changed to round windows to evenly distribute the stress on the glass. Also another glue with a CTE closer to the one of Fused Silica could be used.

Aside from the outcome of the properties of the cell, the gluing process proved to be very informative. It was discovered that a good technique for getting rid of bubbles inside of the glue is to degas the glue in a vacuum. The "piezobrush® PZ3" proved to help increase the adhesion and should for future cells

be used on both the windows and the frame of the cell. Both windows showed rainbow patterns and a lighter color of the glue on one side after baking. One could use a weight that pushes the windows down onto the cell frame, to make sure the glass can not lift off of the frame. Also a better construction for holding the cell horizontal should be build, as the used one probably lead to the glue shifting to one side. When putting the windows down onto the glue, there were also some bubbles trapped. This was possibly caused by the glue not being distributed evenly enough. For distributing the glue more evenly one could use a tool with a bigger width then a syringe, as the syringe can only distribute the glue imprecisely

In conclusion one can say, that even tough the design and the gluing process of the self-glued cell with Fused Silica glass leaves room for improvement to get to a sufficient ER, fused silica glass certainly is a good candidate to reach an UHV for cold atom experiments and provides optical properties, which makes it usable for experiments with small beam sizes.

4.2 Probe and Control Setup

In conclusion it can be said, that the polarization of the 780 nm laser could be set really well with the procedure explained in Section 3.5. The reference construction consisting of a QWP and a polarizer makes the procedure reproducable to set the right polarization as well for the other side of the setup and the 480 nm laser. The polarization could also be well aligned with one of the main axes of a PMF in Section 3.3. An $ER = (2.20 \pm 0.10) \cdot 10^{-3}$ was reached after the fiber, which is good enough.

Regarding the techniques for positioning the optics such that a good optical axis is created, presented in Section 3.4, it was discovered, that the technique of placing the optics with the arducam worked significantly better than placing them with two apertures. It could be seen that the positions of the foci barley changed, when the optics were placed with the arducam. The waist at the foci also always stayed in the constrains mentioned in Section 3.2, but the foci for the vertical and horizontal do not meet in the same place, which has to be corrected. Checking the collimation of the beam, it could be ruled out that a bad collimation of the beam is the reason for this. Seeing that this delocalization could already be seen after placing the lens, it could be concluded, that the position of the mirror or lens is changing the beam foci. The next steps would be to work out, if the mirror is the item relocating the foci or if the light hits the lens in a wrong way. Doing that the new lens mount can be tested as well. After bringing the horizontal and vertical foci together and therefore proving that a construction meeting the constrains can be reproduced even with the additional optics, the whole Rydberg excitation setup can be build around the chamber.

APPENDIX A

Appendix

A.1 Titanium-Fused-Silica-Test-Cell

A.2 Probe and Control Setup

A.3 Useful information

A.3.1 Polarizing and 50/50 Beamsplitter

In this setup the cube beamsplitter "BS005" and the polarizing cube beamsplitter "PBS12-780" by Thorlabs were used. The construction of a BS and PBS can be seen in Fig. A.1. They are made of two glass prism with a dielectric coating between them [34, 43–45]. They work for a specific range of wavelengths as the thickness of the dielectric coating has to be adjusted depending on the wavelength. That is because of the phenomenon called Frustrated Total Internal Reflection (FTIR). Total Internal

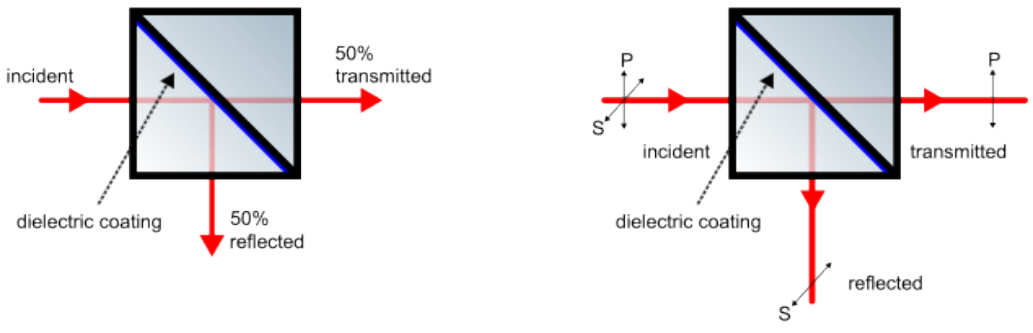

(a) BS (b) PBS

Figure A.1: Construction of a BS and a PBS with light coming in from the left side.

Table A.1: Data of first pumping down the test cell with the turbo pump.

pressure in mbar	time in s
$3.0 \cdot 10^{2}$	25
$1.6 \cdot 10^{1}$	42
$3.0 \cdot 10^{-3}$	68
$4.0 \cdot 10^{-4}$	89
$1.2 \cdot 10^{-4}$	112
$8.6 \cdot 10^{-5}$	127
$6.3 \cdot 10^{-5}$	144
$4.6 \cdot 10^{-5}$	166
$4.0 \cdot 10^{-5}$	183
$3.4 \cdot 10^{-5}$	195
$3.0 \cdot 10^{-5}$	212
$2.5 \cdot 10^{-5}$	237
$2.2 \cdot 10^{-5}$	263
$1.9 \cdot 10^{-5}$	294
$1.6 \cdot 10^{-5}$	339
$1.4 \cdot 10^{-5}$	382
$1.2 \cdot 10^{-5}$	435
$1.0 \cdot 10^{-5}$	498
$8.6 \cdot 10^{-6}$	566
$7.4 \cdot 10^{-6}$	648
$6.3 \cdot 10^{-6}$	755
$5.4 \cdot 10^{-6}$	856
$4.6 \cdot 10^{-6}$	995
$4.0 \cdot 10^{-6}$	1142
$3.0 \cdot 10^{-6}$	1544
$2.2 \cdot 10^{-6}$	2066
$1.6 \cdot 10^{-6}$	2802
$1.4 \cdot 10^{-6}$	3348
$8.6 \cdot 10^{-8}$	59015

Reflection (TIR) happens, when light travels from a medium 1 with a higher refractive index n_1 into a medium 2 with a lower refractive index n_2 at an angle that is bigger that the critical angle. The critical angle can be obtained by taking a look at the law of refraction:

$$\sin(\alpha) = \frac{n_2}{n_1} \sin(\beta)$$

If the light gets transmitted into the medium 2, β has to be smaller than 90° and therefore the sin (β) being smaller than 1. That leads to the following equation for light traveling into the second medium

$$\sin(\alpha) \leq \frac{n_2}{n_1}.$$

The critical angle is now the angle α_g, which is defined by

$$\sin(\alpha_g) = \frac{n_2}{n_1}.$$

So TIR happens for $\alpha \geq \alpha_g$. But it is important, that TIR does not mean, that the wave is not going into the second medium. There are still evanescent waves travelling into the second material. Those waves intensity in medium 2 is $I = I_0 \cdot \exp -x/\lambda$, where I_0 is the initial intensity at $x = 0$ and x is the distance traveled in the second medium. If medium 2 does not absorb, there will still be TIR without any losses to the second medium. But if one brings a second glass prism close to the first one, but medium 2 still between them, one can observe FTIR, if the second prism is closer than a wavelength of the incoming light, as the amplitude of the evanescent wave is still big enough for the light to be transmitted into the second prism. As mentioned before, the amplitude of the evanescent wave at the transition to the second prism is dependent on the wavelength and the thickness of the second medium, in this case the dielectric coating. That is why every beamsplitter has to be tuned to a certain wavelength. By varying the thickness of the coating it can be adjusted how much light gets transmitted and reflected (for the 50/50 BS it is equally devided). The PBS is now different to the BS, as it splits the incoming beam into two differently polarized beams, as seen in Fig. A.1(b). They also work because of the dielectric coating between the two prisms, which reflects s polarized light and transmits p polarized light.

A.3.2 Dichroic Mirror

For the control light a 480 nm laser is used. This has to be directed trough the lens without disturbing the 780 nm light of the Probe laser. To do so the dichroic mirror "DMLP650" from Thorlabs gets used, which reflects light with a wavelength below 650 nm, but transmits light with wavelengths above that.

It does so because of thin-film interference [34, 46]. This can be understood, when looking at the construction of such a mirror in Fig. A.2(a). It consists of a glass substrate with many thin layers of low absorption and different alternating refractive indices. Light hitting those layers gets reflected. The reflected light is maximal, if the reflected partial waves are in phase. The partial waves interfere constructive for certain thicknesses of the layers depending on the wavelength of the incoming light. In Fig. A.2(b) an example with two layers on top of the substrate can be seen, where $n_{air} \leq n_1 \geq n_2 \geq n_3$. Only the light reflected by the first layer does a phase jump of π, as it is reflected by a medium with lower refractive index. To match the phase of this wave and get constructive interference, the first layer has to have the thickness of $\lambda/4$ and the second layer of $\lambda/2$. That is why dichroic mirrors have to be produced for reflecting a specific range of wavelengths at an specific angle. Other wavelengths then do not create constructive interference and get therefore transmitted by the mirror.

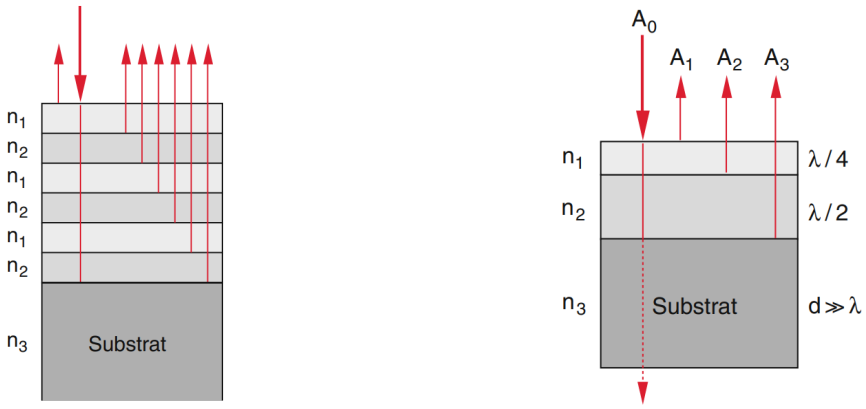

(a) many layers

(b) two layers

Figure A.2: Dichroic mirror with glass substrate and different amounts of layers with different refractive indices [34].

Table A.2: Data of second pumping down the test cell with the turbo pump.

pressure in mbar	time in s
$1.0 \cdot 10^{1}$	34
2.5	43
$1.0 \cdot 10^{-3}$	66
$1.9 \cdot 10^{-4}$	87
$1.0 \cdot 10^{-4}$	103
$7.4 \cdot 10^{-5}$	118
$5.4 \cdot 10^{-5}$	133
$4.6 \cdot 10^{-5}$	145
$4.0 \cdot 10^{-5}$	158
$3.4 \cdot 10^{-5}$	176
$3.0 \cdot 10^{-5}$	198
$2.5 \cdot 10^{-5}$	218
$2.2 \cdot 10^{-5}$	246
$1.9 \cdot 10^{-5}$	279
$1.6 \cdot 10^{-5}$	321
$1.4 \cdot 10^{-5}$	369
$1.2 \cdot 10^{-5}$	427
$1.0 \cdot 10^{-5}$	493
$8.6 \cdot 10^{-6}$	571
$7.4 \cdot 10^{-6}$	659
$6.3 \cdot 10^{-6}$	766
$5.4 \cdot 10^{-6}$	906
$4.6 \cdot 10^{-6}$	1046
$4.0 \cdot 10^{-6}$	1281
$3.4 \cdot 10^{-6}$	1442
$3.0 \cdot 10^{-6}$	1718
$2.5 \cdot 10^{-6}$	2075
$2.2 \cdot 10^{-6}$	2304
$1.9 \cdot 10^{-6}$	2775
$1.6 \cdot 10^{-6}$	3543
$7.4 \cdot 10^{-7}$	8505
$2.5 \cdot 10^{-7}$	70241
$4.0 \cdot 10^{-9}$	616860

Table A.3: Values of fit variables for Gaussian function fits on vertical axis.

	f in a.u.	w(z) in pixels	ρ_0 in pixels
after dichroic mirror	267 000 ± 100	1 369.75 ± 0.80	1 276.65 ± 0.35
after BS	97 550 ± 45	1 377.60 ± 0.80	1 401.65 ± 0.35
after PBS	196 425 ± 95	1 371.20 ± 0.80	1 438.30 ± 0.35
after HWP	198 650 ± 85	1 361.00 ± 0.75	1 453.05 ± 0.35
after QWP	200 370 ± 75	1 366.60 ± 0.65	1 472.60 ± 0.30

Table A.4: Values of fit variables for Gaussian function fits on horizontal axis.

	f in a.u.	w(z) in pixels	ρ_0 in pixels
after dichroic mirror	255 550 ± 100	1 365.65 ± 0.75	1 852.55 ± 0.35
after BS	94 335 ± 65	1 350.5 ± 1.0	1 704.70 ± 0.55
after PBS	190 250 ± 100	1 353.5 ± 1.0	2 121.65 ± 0.50
after HWP	191 050 ± 100	1 344.65 ± 0.95	1 818.85 ± 0.50
after QWP	192 300 ± 100	−1 350.85 ± 0.95	1 823.10 ± 0.50

Table A.5: Converted values of fit variables for Gaussian function fits on vertical axis.

	f in a.u.	w(z) in µm	ρ_0 in µm
after dichroic mirror	267 000 ± 100	2 287.5 ± 1.5	2 132.00 ± 0.65
after BS	97 550 ± 45	2 300.5 ± 1.5	2 340.70 ± 0.60
after PBS	196 425 ± 90	2 290.0 ± 1.5	2 402.00 ± 0.65
after HWP	198 650 ± 85	2 273.0 ± 1.0	2 426.55 ± 0.55
after QWP	200 370 ± 75	2 282.0 ± 1.0	2 459.30 ± 0.50

Table A.6: Converted values of fit variables for Gaussian function fits on horizontal axis.

	f in a.u.	w(z) in µm	ρ_0 in µm
after dichroic mirror	255 550 ± 100	2 280.5 ± 1.0	3 093.70 ± 0.60
after BS	94 335 ± 65	2 255.5 ± 1.5	2 846.90 ± 0.90
after PBS	190 250 ± 100	2 260.0 ± 1.5	3 543.20 ± 0.85
after HWP	191 050 ± 100	2 245.5 ± 1.5	3 037.45 ± 0.80
after QWP	192 300 ± 100	2 256.0 ± 1.5	3 044.5 ± 1.0

Table A.7: Values of fit variables for Eq. (3.6) on vertical axis.

	w_0 in µm	z_0 in µm
after dichroic mirror	8.105 ± 0.040	10 830.5 ± 6.5
after BS	8.300 ± 0.035	10 831.0 ± 5.5
after PBS	8.140 ± 0.035	10 540.5 ± 4.0
after HWP and QWP	8.290 ± 0.030	10 261.5 ± 5.0

Table A.8: Values of fit variables for Eq. (3.6) on horizontal axis.

	w_0 in µm	z_0 in µm
after dichroic mirror	8.390 ± 0.060	10 901.0 ± 8.5
after BS	8.465 ± 0.030	10 902.0 ± 7.0
after PBS	8.405 ± 0.025	10 621.0 ± 6.0
after HWP and QWP	8.465 ± 0.070	10 351.5 ± 5.5

Bibliography

[1] O. Firstenberg, C. S. Adams and S. Hofferberth,
Nonlinear quantum optics mediated by Rydberg interactions,
Journal of Physics B: Atomic, Molecular and Optical Physics **49** (2016) (cit. on p. 1).

[2] M. Saffman, T. G. Walker and K. Mølmer, *Quantum information with Rydberg atoms*,
Rev. Mod. Phys. **82** (3 2010) 2313,
URL: https://link.aps.org/doi/10.1103/RevModPhys.82.2313 (cit. on p. 1).

[3] E. Urban et al., *Observation of Rydberg blockade between two atoms*,
Nature Physics **5** (2009) 110 (cit. on pp. 1, 24).

[4] H. Gorniaczyk, C. Tresp, J. Schmidt, H. Fedder and S. Hofferberth,
Single-Photon Transistor Mediated by Interstate Rydberg Interactions,
Phys. Rev. Lett. **113** (5 2014) 053601,
URL: https://link.aps.org/doi/10.1103/PhysRevLett.113.053601 (cit. on p. 1).

[5] R. Stevenson, J. ř. Miná ř, S. Hofferberth and I. Lesanovsky,
Prospects of charged-oscillator quantum-state generation with Rydberg atoms,
Phys. Rev. A **94** (4 2016) 043813,
URL: https://link.aps.org/doi/10.1103/PhysRevA.94.043813 (cit. on p. 1).

[6] M. Gao, Y.-x. Liu and X.-B. Wang,
Coupling Rydberg atoms to superconducting qubits via nanomechanical resonator,
Phys. Rev. A **83** (2 2011) 022309,
URL: https://link.aps.org/doi/10.1103/PhysRevA.83.022309 (cit. on p. 1).

[7] A. O'Connell et al., *Quantum ground state and single-phonon control of a mechanical resonator*,
Nature **464** (2010) 697 (cit. on p. 1).

[8] T. Nirrengarten et al., *Realization of a Superconducting Atom Chip*,
Phys. Rev. Lett. **97** (20 2006) 200405,
URL: https://link.aps.org/doi/10.1103/PhysRevLett.97.200405 (cit. on p. 1).

[9] K. Bhardwaj, S. Sarkar, S. P. Ram, V. B. Tiwari and S. R. Mishra,
A method for loading magneto-optical trap in an ultrahigh vacuum environment,
API Advances **13** (1 2023) 200405 (cit. on pp. 1, 38).

[10] R. Grimm, M. Weidemüller and Y. B. Ovchinnikov, "Optical Dipole Traps for Neutral Atoms", ed. by B. Bederson and H. Walther, vol. 42, Advances In Atomic, Molecular, and Optical Physics, Academic Press, 2000 95,
URL: https://www.sciencedirect.com/science/article/pii/S1049250X0860186X (cit. on p. 1).

[11] Newport Corporation, *Optical Materials*,
URL: https://www.newport.com/n/optical-materials (visited on 07/09/2023) (cit. on pp. 1, 4, 5).

[12] S. Germer, *Frequency stabilization of a laser and a high resolution optical setup for excitation of ultracold Rydberg atoms*, 2023 (cit. on pp. 2, 24, 26, 28, 30, 31).

[13] *Vacuum Technology Book Volume II*, Pfeiffer Vacuum GmbH, 2013 (cit. on pp. 3–5).

[14] Infleqtion, *Atomic Prisms, UHV Glass Cells*,
URL: https://www.infleqtion.com/atomic-prisms (visited on 18/09/2023) (cit. on pp. 3, 4).

[15] Pfeiffer Vacuum GmbH, *Viewports*,
URL: https://www.pfeiffer-vacuum.com/en/know-how/mechanical-components-in-vacuum/components-and-feedthroughs/viewports/ (visited on 18/09/2023) (cit. on p. 3).

[16] Epoxy Technoloy Inc., *EPO-TEK H77S*,
URL: https://www.epotek.com/docs/en/Datasheet/H77S.pdf (visited on 07/09/2023) (cit. on pp. 5, 7, 10, 11).

[17] Rosen Metall-Service GmbH, *WERKSTOFFDATENBLATT - Titan Grade 2*,
URL: https://rosen-metall.de/fileadmin/Werkstoffdatenblaetter/Sonderwerkstoffe/Werkstoffdatenblatt_TiG2.pdf (visited on 07/09/2023) (cit. on pp. 5, 11).

[18] Präzisions Glas & Optik GmbH, *N-BK7*,
URL: https://www.pgo-online.com/de/BK7.html (visited on 07/09/2023) (cit. on p. 5).

[19] Heraeus Holding, *Properties of fused silica*,
URL: https://www.heraeus.com/en/hca/fused_silica_quartz_knowledge_base_1/properties_1/properties_hca.html#tabs-608478-5 (visited on 13/09/2023) (cit. on pp. 5, 11).

[20] K. M. Birnbaum and T. Q. O. Group, *Ultra-High Vacuum Chambers*, 2005 (cit. on pp. 6, 7).

[21] *Product information, Sonoswiss Cleaner T1 (SW-C T1)*, Sonoswiss AG, 2018 (cit. on p. 6).

[22] *Product information, Sonoswiss Cleaner T2 (SW-C T2)*, Sonoswiss AG, 2018 (cit. on p. 6).

[23] Epoxy Europe, *Chemistry Basics*,
URL: https://epoxy-europe.eu/epoxies/chemistry-basics/#:~:text=The%20most%20common%20epoxy%20resins,known%20as%20BADGE%20or%20DGEBA. (visited on 11/09/2023) (cit. on p. 7).

[24] technicoll®, *Two-component adhesives, characteristics and application*,
URL: https://www.technicoll.eu/adhesive-knowledge/two-component-adhesives.html (visited on 11/09/2023) (cit. on p. 7).

[25] RELYON PLASMA GMBH, *Atmosphärendruckplasma zur Oberflächenbehandlung*, URL: https://www.relyon-plasma.com/glossary/atmosphaerendruckplasma/ (visited on 12/09/2023) (cit. on p. 9).

[26] RELYON PLASMA GMBH, *Plasma activation for surface activation and modification*, URL: https://www.relyon-plasma.com/plasma-activation/?lang=en (visited on 12/09/2023) (cit. on p. 9).

[27] RELYON PLASMA GMBH, *piezobrush® PZ3, Effective plasma handheld device for manual use*, URL: https://www.relyon-plasma.com/piezobrush-pz3/?lang=en (visited on 12/09/2023) (cit. on p. 9).

[28] RELYON PLASMA GMBH, *Surface tension and surface energy improved by plasma treatment*, URL: https://www.relyon-plasma.com/glossary/surface-tensions-and-surface-energy/?lang=en (visited on 12/09/2023) (cit. on p. 9).

[29] RELYON PLASMA GMBH, *Oberflächenbehandlung mit Plasma, Optimierung Bentzung*, URL: https://www.relyon-plasma.com/glossary/oberflaechenbehandlung-mit-plasma/ (visited on 12/09/2023) (cit. on p. 9).

[30] Pfeiffer Vacuum GmbH, *ActiveLine Gauges*, URL: https://www.pfeiffer-vacuum.com/en/products/measurement-analysis/measurement/activeline/activeline-gauges/15936/pkr-360-low-current-dn-40-cf-f (visited on 03/10/2023) (cit. on p. 13).

[31] Stanford Research Systems, *Vacuum Diagnosis with an RGA, Application Note 7*, URL: https://www.thinksrs.com/downloads/pdfs/other%20stuff/RGA_vac_diag.pdf (visited on 14/09/2023) (cit. on p. 14).

[32] Hessisches Landesamt für Naturschutz, Umwelt und Geologie, *Grundlagen, Zusammensetzung der Luft*, URL: https://www.hlnug.de/themen/luft/grundlagen#:~:text=Zusammensetzung%20der%20Luft,ein%20(Global%20Monitoring%20Laboratory)%20. (visited on 15/09/2023) (cit. on p. 14).

[33] allectra, *HIGH VACUUM LEAK SEALANT (VACSEAL)*, URL: https://shop.allectra.com/products/330-VACSEAL-S (visited on 15/09/2023) (cit. on p. 15).

[34] W. Demtröder, *Experimentalphysik 2: Elektrizität und Optik*, 6th ed., Springer, 2013, ISBN: 978-3-642-29944-5 (cit. on pp. 18, 24, 27, 40, 42, 43).

[35] Wikipedia, *Birefringence*, URL: https://en.wikipedia.org/wiki/Birefringence#:~:text=Birefringence%20is%20the%20optical%20property,be%20birefringent%20(or%20birefractive). (visited on 04/10/2023) (cit. on p. 18).

[36] D. Meschede, *Optik, Licht und Laser*, 3rd ed., Vieweg+Teubner, 2008, ISBN: 978-3-8351-0143-2 (cit. on p. 20).

[37] D. A. Steck, *Rubidium 87 D Line Data*, Los Alamos National Laboratory, 2001 (cit. on p. 21).

[38] A. Paris-Mandoki et al., *Free-Space Quantum Electrodynamics with a Single Rydberg Superatom*, Phys. Rev. X **7** (4 2017) 041010, URL: https://link.aps.org/doi/10.1103/PhysRevX.7.041010 (cit. on p. 21).

[39] P. Bernasconi, *Characterization of Polarization Maintaining Fiber Optic Components*, (2016), URL: https://www.diamond-fo.com/fileadmin/user_upload/Content/Extranet/Documents_and_Downloads/White_Papers_Product_release_and_Newsletter/English/WP_Characterization_of_PM_Components.pdf (cit. on p. 25).

[40] G. B. Malykin, *Use of the poincare sphere in polarization optics and classical and quantum mechanics. Review*, Radiophysics and Quantum Electronics, 1997 (cit. on p. 33).

[41] M. H. Anderson, J. R. Ensher, M. R. Matthews, C. E. Wieman and E. A. Cornell, *Observation of Bose-Einstein Condensation in a Dilute Atomic Vapor*, Science **269** (5221 1995) 198 (cit. on p. 38).

[42] K. B. Davis et al., *Bose-Einstein Condensation in a Gas of Sodium Atoms*, Phys. Rev. Lett. **75** (22 1995) 3969, URL: https://link.aps.org/doi/10.1103/PhysRevLett.75.3969 (cit. on p. 38).

[43] Wikipedia, *Beam splitter*, URL: https://en.wikipedia.org/wiki/Beam_splitter (visited on 24/09/2023) (cit. on p. 40).

[44] Wikipedia, *Total internal reflection*, URL: https://en.wikipedia.org/wiki/Total_internal_reflection (visited on 24/09/2023) (cit. on p. 40).

[45] Edmund Optics Inc., *What are beamsplitters?*, URL: https://www.edmundoptics.com/knowledge-center/application-notes/optics/what-are-beamsplitters/ (visited on 24/09/2023) (cit. on p. 40).

[46] Wikipedia, *Dichroic filter*, URL: https://en.wikipedia.org/wiki/Dichroic_filter (visited on 25/09/2023) (cit. on p. 42).

List of Figures

List of Tables